RSC Advances

ROYAL SOCIETY OF CHEMISTRY

PAPER

View Article Online
View Journal | View Issue

Check for updates

Cite this: *RSC Adv.*, 2026, **16**, 20658

Eco-safe degradation of reactive orange 16 *via* adsorption-enhanced photocatalysis using $CoFe_2O_4$ nanoparticles

Nasira Hussain,[a] Muhammad Bilal, *[b] Muhammad Younas Afzal,[a] Shanza Shafaat,[a] Bilal Ahmad Zafar Amin,[c] Faheem Shah *[d] and Ahson Jabbar Shaikh *[a]

Received 12th March 2026
Accepted 13th April 2026

DOI: 10.1039/d6ra02108e

rsc.li/rsc-advances

The increasing release of synthetic azo dyes into aquatic systems demands efficient, low-cost, and sustainable remediation strategies. In this study, cobalt ferrite ($CoFe_2O_4$) nanoparticles were synthesized *via* the co-precipitation method and applied for the adsorption-assisted photocatalytic removal of Reactive Orange 16 (RO16) dye. The nanoparticles exhibited a mesoporous morphology (average pore diameter 13.32 nm; specific surface area 26.98 $m^2\ g^{-1}$) and a narrow optical band gap of 2.91 eV, ensuring strong visible-light activity. Adsorption experiments revealed a maximum dye uptake of 112.3 mg g^{-1}, with equilibrium data best fitting the Freundlich and Redlich–Peterson models, confirming heterogeneous multilayer adsorption. Kinetic modeling indicated a pseudo-second-order rate mechanism, whereas thermodynamic parameters ($\Delta H = 51$ kJ mol^{-1}; $\Delta G < 0$) indicated that the process is endothermic and spontaneous. Under visible irradiation, $CoFe_2O_4$ NPs achieved up to 83.5% photodegradation efficiency at pH 2, following pseudo-first-order kinetics. The integrated adsorption–photocatalysis mechanism involved synergistic electrostatic, π–π, and hydroxyl radical interactions, leading to effective decolorization and mineralization. AI-based Shapley Additive Explanations (SHAP) and Principal Component Analysis (PCA) analyses validated experimental results, identifying contact time and initial concentration as the dominant factors governing removal efficiency. Phytotoxicity and antibacterial studies confirmed the eco-safe nature of $CoFe_2O_4$ NPs, with over 90% tomato seed germination and no toxic bacterial response. This work presents a dual-functional, environmentally friendly nanomaterial capable of coupling adsorption and photocatalysis for the sustainable removal of complex dye pollutants.

Introduction

Industrial development in any country plays a central role in economic progress, but simultaneously escalates environmental pollution, particularly water contamination.[1] Synthetic dyes released by the textile, leather, paper, and plastic industries are considered among the most harmful and persistent. Azo dyes are the most important and the largest class of commercial dyes, and they represent almost 65–75% of all products of textile dyes. They are chemically stable, water-soluble, and difficult to degrade, making their removal from wastewater a big challenge.[2] An additional reason for concern about azo dyes is the risk of exposure to potentially carcinogenic aromatic amines, formed throughout the metabolic cleavage of the azo linkage.[3] Reactive orange 16 (RO16) is usually utilized in textile dyeing processes and owing to its complex aromatic structure and resistance to biodegradation, it frequently escapes conventional treatment methods. Its presence in aquatic systems poses acute risks to both aesthetic and toxicological aspects by obstructing light penetration, reducing dissolved oxygen, and endangering aquatic organisms. Furthermore, RO16 and its degradation byproducts, like aromatic amines, have shown mutagenic, carcinogenic, and allergenic effects in humans, raising public health issues.[4]

As the demand for wastewater treatment in a better and more sustainable way rises around the world, it's important to discover methods for removing dyes from water that are low-cost and harmless for the environment. Even though techniques such as coagulation, ozonation, and membrane filtration have been utilized to treat dye-laden waste, they undergo from various limitations like clogging, time-consuming, and high energy input.[5] Among these wastewater treatment technologies, adsorption,[6–9] photocatalysis,[10] and membrane

---

[a] Department of Chemistry, COMSATS University Islamabad, Abbottabad Campus, Abbottabad 22060, KPK, Pakistan. E-mail: ahson@cuiatd.edu.pk; Fax: +92-(0)992-383-441; Tel: +92-(0)334-377-0104

[b] Department of Environmental Sciences, COMSATS University Islamabad, Abbottabad Campus, Abbottabad 22060, KPK, Pakistan. E-mail: mbilal@cuiatd.edu.pk; Fax: +92-(0)992-383-441; Tel: +92-333-541-1536

[c] Department of Chemical Engineering, COMSATS University Islamabad – Lahore Campus, Lahore, Punjab, Pakistan

[d] Department of Chemistry, College of Science, King Faisal University, Hofuf, Eastern Province AlAhsa 31982, Kingdom of Saudi Arabia. E-mail: fshah@kfu.edu.sa; Tel: +966-530-801-618

processes[11] are showing encouraging results. Among these, adsorption is considered one of the most effective and economical methods for dye removal due to its simplicity, high efficiency, and ability to treat low-concentration pollutants. It operates through the interaction between dye molecules and the surface of an adsorbent, offering easy operation, reusability of materials, and minimal formation of harmful by-products. Photocatalytic oxidation, a water treatment process that emerged in the 1970s, has attracted considerable attention due to its potential for the efficient and sustainable removal of pollutants from wastewater.[12] The synergistic integration of adsorption and photocatalysis, often referred to as adsorption-assisted photocatalysis, has gained remarkable attention, as it combines the high pollutant uptake capacity of adsorption with the strong oxidative degradation ability of photocatalysis, ensuring both efficient dye removal and complete mineralization. The main advantages are that photocatalysis could be carried out under ambient conditions, does not involve mass transfer, and can also lead to total transformation of organic carbon to CO_2.[13] However, the performance largely depends on the nature and properties of the adsorbent material. Various nanoparticles have been investigated for environmental remediation due to the ease of changing their surface functionality and their high surface-to-volume ratio for increased adsorption capacity and efficiency. Nanosized metal oxides, such as manganese oxides, aluminum oxides, magnesium oxides, and cerium oxides, are thought to be capable of adsorbing dyes from aqueous solutions. They have a number of advantages, including high chemical stability, unsaturated surfaces, ease of use, quick kinetics, and favorable dye adsorption in water and wastewater.[14] Currently, ferrites are well recognized in the area of different types of wastewater treatment for pollutant removal *via* adsorption and photodegradation. As these ferrites mostly have high surface area to volume ration, excellent chemical stability and ecofriendly nature. Among these, cobalt ferrite ($CoFe_2O_4$) has attracted significant attention. $CoFe_2O_4$ is a spinel-structured magnetic nanomaterial characterized by high thermal and chemical stability, ferromagnetic and a high degree of surface functionalization potential.[15] These properties make it a good choice for environmental remediation procedures. The magnetic nature allows for easy recovery of the adsorbent after treatment using a simple external magnet, addressing the separation limitations of conventional adsorbents. These NPs also exhibit strong light absorption and high photostability, allowing effective degradation of organic dyes under irradiation. Moreover, the synthesis of $CoFe_2O_4$ nanoparticles is relatively straightforward and cost-effective, involving co-precipitation methods that are scalable and reproducible.

In recent years machine learning (ML) approaches have emerged as powerful tools for analyzing adsorption processes. Traditional kinetic and isotherm models provide mechanistic insights but are often limited in capturing complex, nonlinear interactions between multiple experimental variables such as pH, contact time, temperature, adsorbent dose, and initial concentration. AI-based models, particularly those using explainable tools like SHAP (SHapley Additive exPlanations) and PCA (Principal Component Analysis), allow for deeper interpretation of parameter influence and correlations. Such analyses not only validate experimental findings but also help in prioritizing parameters, identifying hidden patterns, and improving process optimization for dye removal. Integrating AI-based evaluation with experimental data strengthens the predictive capacity of adsorption systems and supports the development of scalable water treatment strategies.

Although $CoFe_2O_4$ NPs have been extensively investigated for dye removal, most previous studies have primarily focused on either adsorption or photocatalysis, often neglecting the integration of both processes and their comprehensive evaluation. The present study uniquely combines adsorptive-assisted photocatalysis with AI-driven data interpretation and eco-safety validation, thereby bridging critical gaps in current research. The synthesized $CoFe_2O_4$ NPs exhibited excellent structural and surface properties, showing high adsorption capacity (112.3 mg g^{-1}) and eco-safety, supporting their suitability for sustainable azo dye remediation. Furthermore, AI-based modeling tools, including SHAP, PCA, and correlation analysis, were employed to interpret and predict the influence of key operational parameters (pH, contact time, adsorbent dose, temperature, and concentration) on dye removal efficiency. This dual experimental computational framework not only validates the adsorption performance of $CoFe_2O_4$ NPs but also provides mechanistic insight and predictive capability for process optimization. By coupling adsorption with photocatalysis, the study advances a synergistic adsorption-assisted photocatalytic approach that enhances RO16 degradation efficiency while ensuring process sustainability. Overall, this research establishes eco-safe and intelligent hybrid treatment strategy, integrating adsorption, photocatalysis, and artificial intelligence to achieve efficient and sustainable remediation of dye-contaminated wastewater.

Materials and methods

Iron(III) chloride hexahydrate ($FeCl_3 \cdot 6H_2O$), cobalt chloride dihydrate ($CoCl_2 \cdot 2H_2O$), hydrochloric acid (HCl), and sodium hydroxide (NaOH) were purchased from Dae-Jung Chemicals and Metals Co. Ltd, Republic of Korea. Tomato seeds were purchased from local market. Reactive orange 16 (99%) of analytical grade was bought from Merck Germany. All the reagents were employed without any further purification and solutions were prepared in distilled water. A 1000 mg per L stock solution of RO16 dye was prepared by dissolving 1 g of dye in distilled water and then making up the total volume to 1 L. The appropriate stock solution dilution with distilled water leads to various dye solution concentrations.

Synthesis of cobalt ferrite ($CoFe_2O_4$) nanoparticles

$CoFe_2O_4$ NPs were synthesized by co-precipitation method.[16] The stoichiometric amounts of 0.4 M ferric chloride hexahydrate ($FeCl_3 \cdot 6H_2O$) and 0.2 M cobalt chloride hexahydrate ($CoCl_2 \cdot 6H_2O$) were each prepared separately in 20 mL of distilled water, and the two solutions were then combined 1 M

NaOH was added dropwise into the above solution as precipitating agent, and it increased the pH of the solution up to 12.

The solution turned dark brown. To facilitate the formation of precipitates, the mixture was stirred at 1000 rpm for 2 h at 70 °C. Afterwards, the precipitates were collected by centrifugation at 6000 rpm, washed three times with distilled water, and then dried in an oven at 100 °C for 2 h. Finally, the washed and dried precipitates were calcined at 400 °C for 4 h in a muffle furnace.[17]

$CoFe_2O_4$ NPs characterization

The functional groups of the $CoFe_2O_4$ NPs, and $CoFe_2O_4$ NPs adsorbed RO16 dye were identified using Fourier transform infrared spectroscopy. Fourier Transform Infrared (FTIR) spectra were recorded using a Bruker Alpha-2 spectrometer in the spectral range of 4000–400 cm^{-1} with a resolution of 4 cm^{-1} and 32 scans. The morphology of the $CoFe_2O_4$ nanoparticles (NPs) was investigated using a scanning electron microscope (SEM). The surface morphology of the samples was examined using scanning electron microscope. Prior to analysis, the samples were finely powdered and mounted on aluminum stubs using double-sided carbon adhesive tape. To improve conductivity and prevent charging, the samples were sputter-coated with a thin layer of gold under vacuum. The SEM images were recorded at an accelerating voltage of 10–20 kV. The surface area, pore size, and pore volume of the samples were measured using Brunauer–Emmett–Teller (BET) analysis. Nitrogen adsorption–desorption measurements were performed using a Micromeritics ASAP 2460 surface area and porosity analyzer. Approximately 100 mg of sample was degassed at 300 °C for 6 h prior to analysis to remove moisture and impurities. The hydrodynamic size of the $CoFe_2O_4$ NPs, which represents the size of the NPs along with the surrounding solvent layer, was measured using dynamic light scattering (DLS). Zeta potential analysis afforded details of the stabilization of $CoFe_2O_4$ NPs measured at room temperature (RT; 25 °C) on a Zeta sizer Nano ZSP (Malvern Instruments, Malvern, UK) using ZETA SIZER software (8.02). For analysis, 1 mg of the sample was dispersed in 10 mL of deionized water and ultrasonicated for 15 minutes to obtain a homogeneous suspension. The suspension was transferred into a capillary cell, and measurements were performed at neutral pH. Each sample was analyzed in triplicate, and the average value was reported.

Batch adsorption experiment

The batch adsorption experiment was used to study the efficiency of $CoFe_2O_4$ NPs for RO16 dye removal. Various experimental conditions were applied to obtain the optimal range of adsorption. A known amount of $CoFe_2O_4$ NPs was added to the flasks containing RO16 dye solution (35 mL). These flasks were agitated at a fixed shaking speed of 200 rpm in a temperature-controlled orbital shaker at 35 °C. After reaching equilibrium, the solution was separated from NPs through centrifugation. Ultimately, the concentrations of residual RO16 dye were determined by UV-Vis spectroscopy at λ_{max} 496 nm. First a reagent blank was processed in the same manner. The study investigated the impact of varying parameters, including contact times ranging from 10 to 120 minutes, adsorbent dose (ranging from 0.25 to 2 mg), pH levels (including 2, 6, 8, and 10), and initial concentrations (ranging from 10 to 500 mg L^{-1}). The pH of the solution was adjusted by using 0.1 M HCl and 0.1 M NaOH. The dye concentrations were measured using a UV-Vis spectrophotometer at the wavelength of its maximum absorbance, λ_{max} of 496 nm. Using the Beer–Lambert equation, the final dye concentration was measured by a spectrophotometer to correspond to the dye's maximum concentration. A pH meter was used to determine the pH of the dye solution. Eqn (1) and (2) were used to calculate the adsorption capacity (q_e) and % dye removal.

$$\%R = \left(\frac{C_0 - C_t}{C_0}\right) \times 100 \quad (1)$$

$$q_t = \left(\frac{C_0 - C_t}{m}\right) \times V \quad (2)$$

Here, C_0 and C_t in mg L^{-1} are the initial dye concentration and the dye concentration at time, V (mL) is the volume of the RO16 dye solution, and m (g) corresponds to the mass of the NPs. All experiments were performed in triplicate to ensure reproducibility, and the error bars in the plots represent the standard deviation of the measurements. A detailed study of adsorption isotherms, kinetics, and thermodynamic analysis is provided in the SI.

Photocatalytic degradation experiment

The photocatalytic activity of the synthesized $CoFe_2O_4$ nanoparticles (NPs) was evaluated by monitoring the degradation of RO16 dye under visible light irradiation. A known amount of catalyst was added to a fixed volume of dye solution and stirred in the dark for 30 minutes to attain adsorption–desorption equilibrium. Afterward, the suspension was exposed to UV light under continuous stirring. At specific time intervals, aliquots were withdrawn, centrifuged to separate the photocatalyst, and analyzed using a UV-Vis spectrophotometer to measure the remaining dye concentration.

Active species trapping studies

Under similar conditions, the radical-trapping studies were like those for RO16 photocatalytic degradation. Different scavengers, including EDTA (ethylene diamine tetra-acetate) (h^+-scavenger), silver nitrate ($AgNO_3$) (e^--scavenger), and *n*-propyl alcohol ($\cdot OH$-scavenger). The study was conducted by adding 0.01 and 0.02 M of each scavenger to the dye solution before adding the photocatalyst.

AI-based data analysis

The experimental adsorption data for RO16 dye removal using $CoFe_2O_4$ nanoparticles were analyzed using Python (version 3.9) with scientific computing libraries including pandas, NumPy, scikit-learn, SHAP, matplotlib, and seaborn. All computational analyses were performed on the same workstation used for previous modeling studies to maintain consistency in data processing and visualization workflows. Prior to analysis, the dataset was organized in tabular format and screened for missing values and outliers. The experimental parameters including solution pH, contact time, temperature, adsorbent dosage, and initial dye concentration were used as input variables, while the percentage removal efficiency (% removal) served as the response variable. To ensure comparable scaling and improve model stability, input features were normalized using standard feature scaling. A Gradient Boosting Regressor (GBR) model implemented in the scikit-learn library was employed to capture nonlinear relationships between operational parameters and adsorption performance. The dataset was divided into training and validation subsets to evaluate model reliability and prevent overfitting.

To interpret the machine learning model and quantify the influence of individual experimental parameters, SHapley Additive exPlanations (SHAP) analysis was conducted. SHAP values enabled identification of both positive and negative contributions of each variable to the adsorption efficiency, providing interpretable insights into the relative importance and interaction of operational parameters. Additionally, Principal Component Analysis (PCA) was performed using the scikit-learn library to reduce data dimensionality and identify underlying patterns among experimental conditions. PCA projections facilitated visualization of dominant trends and clustering behavior within the adsorption dataset. To further examine relationships among experimental variables, Pearson correlation coefficients were calculated and visualized using seaborn heatmaps, enabling rapid identification of linear associations between parameters and adsorption performance. The integration of machine learning modeling, SHAP interpretability analysis, and multivariate statistical methods provided a comprehensive computational framework to complement experimental observations and improve understanding of the adsorption mechanism governing RO16 dye removal using $CoFe_2O_4$ nanoparticles.

Phototoxicity and antibacterial activity

Tomato seeds (20 seeds per Petri dish) were surface-sterilized by immersing them in 70% ethanol for 1 min, followed by a 10 min treatment with a 30% (v/v) solution of commercial bleach (sodium hypochlorite, ~5–6% active chlorine), and then rinsed thoroughly with distilled water. The sterilized seeds were treated at 4 °C for 24 hours for cold stratification. All materials, including Petri dishes, filter papers, forceps, and distilled water, were sterilized by autoclaving. Treated and control solutions were employed to check the phytotoxic effects on seed germination under controlled environment. The antibacterial potential of the synthesized cobalt ferrite ($CoFe_2O_4$) NPs was evaluated using the agar well diffusion method as described in the literature.[18] *Pseudomonas aeruginosa* PAO1 was selected as the test microorganism. The bacterial strain was cultured in Luria-Bertani (LB) broth and maintained on LB agar plates. Fresh bacterial suspension equivalent to 0.5 McFarland standard (approximately 1×10^8 CFU mL^{-1}) was uniformly spread on the surface of sterile LB agar plates using a sterile cotton swab. Wells of 6 mm diameter were punched aseptically into the agar using a sterile cork borer, and 100 µL of nanoparticle suspension (at predetermined concentration) was loaded into each well. The plates were incubated at 37 °C for 24 hours. Kanamycin (1 mg mL^{-1}) was used as positive control, while sterile distilled water served as the negative control.

Results and discussions

$CoFe_2O_4$ nanoparticles characterization

UV-visible spectra, Tauc plot, photoluminescence spectra, and X-ray diffraction spectra. The UV-Vis absorption spectrum of $CoFe_2O_4$ NPs shown in Fig. 1a exhibits absorption band at 264 nm 452 nm and 759 nm, indicating electronic transitions corresponding to metal–ligand charge transfer and d–d transitions of Fe^{3+} and Co^{2+} ions. Tauc plot in Fig. 1b, which is derived from the UV-Vis spectrum, is used to determine the optical band gap of $CoFe_2O_4$ NPs. The Tauc relation, $(\alpha h\nu)^n = A(h\nu - E_g)$, where α is the absorption coefficient, $h\nu$ is photon energy, and E_g is the optical band gap, helps in estimating the band gap energy. E_g value depended on various factors, including lattice strain, carrier concentration and crystallite size. By extrapolating the linear region of the Tauc plot to the x-axis, the estimated band gap of 2.91 eV was determined for $CoFe_2O_4$ NPs. In another study band gap energies of same material were observed as 2.1 eV.[19] Fig. 1c demonstrates the photoluminescence spectra (PL). An excitation wavelength of 325 nm was chosen to efficiently excite a broad range of electronic states and defect levels. Similar UV excitation wavelengths have been employed in previous photoluminescence studies of ferrite nanomaterials to generate strong emission signals for analysis.[20,21] The PL spectrum exhibits multiple emission peaks at approximately 422 nm, 432 nm, 444 nm, 483 nm, 528 and 568 nm, indicating the existence of different energy states and defect-related emissions within the NPs. The predominant peak appears at 422 nm is the result of free electrons intensely trapped at the holes generated by the photons in the oxygen vacancies.[22] The emission peaks observed at 432 nm and 444 nm correspond to near-band-edge emission, which is associated with the recombination of excitons. The blue emission peak was observed at the 460 nm is attributed to the Fe^{3+} transition in the ferrite sites.[23] Peaks at 528 nm and 568 nm are typically attributed to deep-level or defect-related emissions, which are often due to oxygen vacancies, interstitials, or other surface states within the ferrite structure. The crystal structure and phase purity of the as-synthesized $CoFe_2O_4$ NPs were investigated using XRD. The pattern, presented in Fig. 1d, confirms the successful formation of the cubic spinel structure. The main diffraction peaks observed at 2θ values correspond to the (220), (311), (222), (400), (422), and (511) crystal planes. These characteristic reflections are consistent with the standard powder diffraction data for cubic $CoFe_2O_4$ nanoparticles (NPs).[24]

Brunauer–Emmett–Teller (BET) surface analysis of $CoFe_2O_4$ NPs. Each sample weighing 100 mg, underwent initial degassing at 300 °C for 6 h to eliminate surface impurities and water. Subsequently, the N_2 adsorption and desorption process was

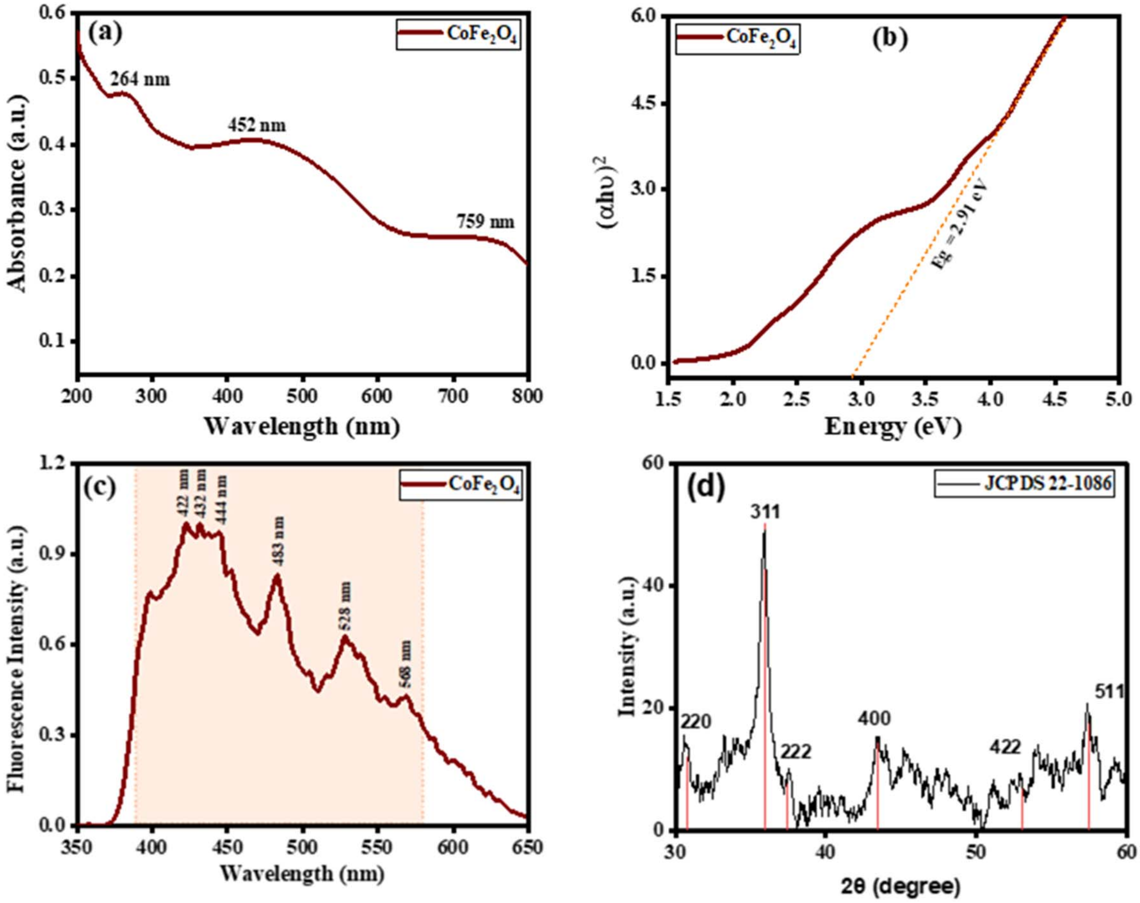

Fig. 1 Characterization of $CoFe_2O_4$ nanoparticles (NPs): (a) UV-visible absorption spectra, (b) Tauc plot for determination of direct band gap, (c) photoluminescence (PL) spectra, and (d) X-ray diffraction (XRD) pattern.

conducted at −196 °C using a physical adsorption analyzer, and the sample's surface area was determined using the Brunauer–Emmett–Teller (BET) theory. The total pore volume and pore size distribution were determined using the Barrett–Joyner–Halenda (BJH) algorithm. The isotherm exhibits a typical type IV behavior with an H3 hysteresis loop, characteristic of mesoporous materials.[25] The adsorption and desorption curves closely follow each other, suggesting uniform pore distribution. The BET surface area of $CoFe_2O_4$ NPs was calculated to be 26.98 $m^2\ g^{-1}$, while the total pore volume was 0.11 $cm^3\ g^{-1}$, as shown in Fig. 2a. Fig. 2b represents the Barrett–Joyner–Halenda (BJH) pore size distribution, indicating an average pore diameter of 13.32 nm, further confirming the mesoporous nature of the NPs. These porosity characteristics play a crucial role in the adsorption performance of $CoFe_2O_4$ NPs providing ample active sites for dye molecule interactions.

FTIR spectra and hydrodynamic size of $CoFe_2O_4$ NPs before and after dye adsorption. FTIR spectra of $CoFe_2O_4$ NPs before and after the adsorption of RO16 dye provides insight into the functional groups involved in the adsorption process are shown in Fig. 3a and b. The spectrum before adsorption exhibits peaks at 495 cm^{-1}, corresponding to stretching and bending vibrations of the M–O bonds in tetrahedral and octahedral sites of spinel ferrites.[26] A broad peak around 3470 cm^{-1} is attributed to the O–H stretching vibration of hydroxyl groups, while a peak at 1640 cm^{-1} corresponds to H–O–H bending from adsorbed water.[27] These results are consistent with those reported in the literature.[28] After adsorption, noticeable changes are observed in the FTIR spectrum. New peaks emerge in the 1000–1300 cm^{-1} range, corresponding S═O stretching vibration confirming the presence of sulfonate groups from the dye. The appearance of peaks at 1400–1660 cm^{-1} suggests the presence of C═C stretching vibrations from the poly aromatic ring of RO16 dye.[29] These spectral changes confirm the successful adsorption of RO16 onto $CoFe_2O_4$ NPs. Hydrodynamic size[30] of $CoFe_2O_4$ NPs before am dater RO16 dye adsorption is demonstrated in Fig. 3c. It is observed that the $CoFe_2O_4$ NPs exhibit hydrodynamic size of 142 nm, and after adsorption of RO16 size slightly increases to 210 nm. This value is relatively larger than particle size calculated from SEM, which is attributed to several contributing factors. DLS measures the hydrodynamic diameter, which represents not only the core nanoparticle but also includes the solvation layer and any surface-adsorbed ions or molecules from the aqueous dispersion medium. Hence, the solvent effect (due to water molecules and surface hydroxyl groups forming a hydration shell) leads to an apparent increase in particle size.[31] Aggregation in suspension also contributes to the larger DLS-measured size.[32]

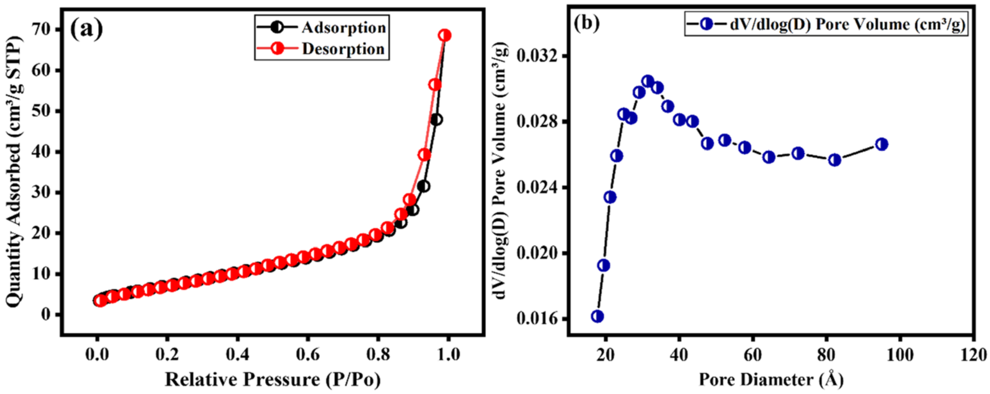

Fig. 2 Porous properties of $CoFe_2O_4$ NPs: (a) Brunauer–Emmett–Teller (BET) surface area analysis, and (b) pore size distribution.

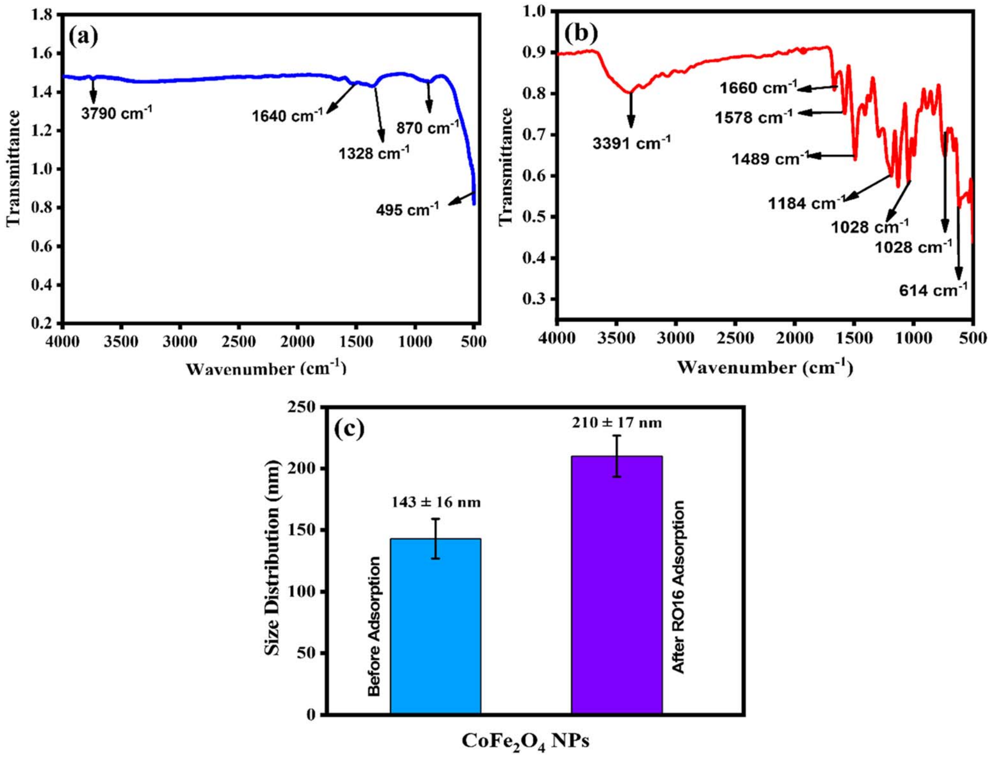

Fig. 3 Structural and size analysis of $CoFe_2O_4$ NPs before and after RO16 dye adsorption: (a) FTIR spectra before adsorption, (b) FTIR spectra after adsorption, and (c) hydrodynamic size distribution measured by DLS.

SEM analysis of $CoFe_2O_4$ NPs before and after dye adsorption. Fig. 4a depicts the SEM image of $CoFe_2O_4$ NPs showing a agglomerated, nano-grained structure with irregular shapes. The NPs were evenly distributed throughout the sample and were nearly spherical in size. According to the findings of SEM analysis, $CoFe_2O_4$ particles have a non-uniform and heterogeneous morphology because of the magnetic force's agglomeration.[33] The particle size calculated by image J as shown in Fig. 4b was 35 nm. In contrast, after dye adsorption in Fig. 4c, the NPs appeared rougher surface morphology, indicating the deposition of dye molecules onto the adsorbent surface. These structural modifications suggest successful adsorption of dye onto $CoFe_2O_4$ NPs. The particle size calculated was 62 nm as shown in Fig. 4d. Confirmation of dye attachment was also confirmed through FTIR as discussed above in Fig. 3b, where the appearance of new peaks corresponding to dye functional groups was observed.

Effect of adsorption parameters on dye removal

Effect of contact time, concentration of RO16 dye and $CoFe_2O_4$ NPs dose. The equilibrium time is essential when considering economical water and wastewater applications, and contact time is an important component in all transfer phenomena for the adsorption process.[14] Adsorption process

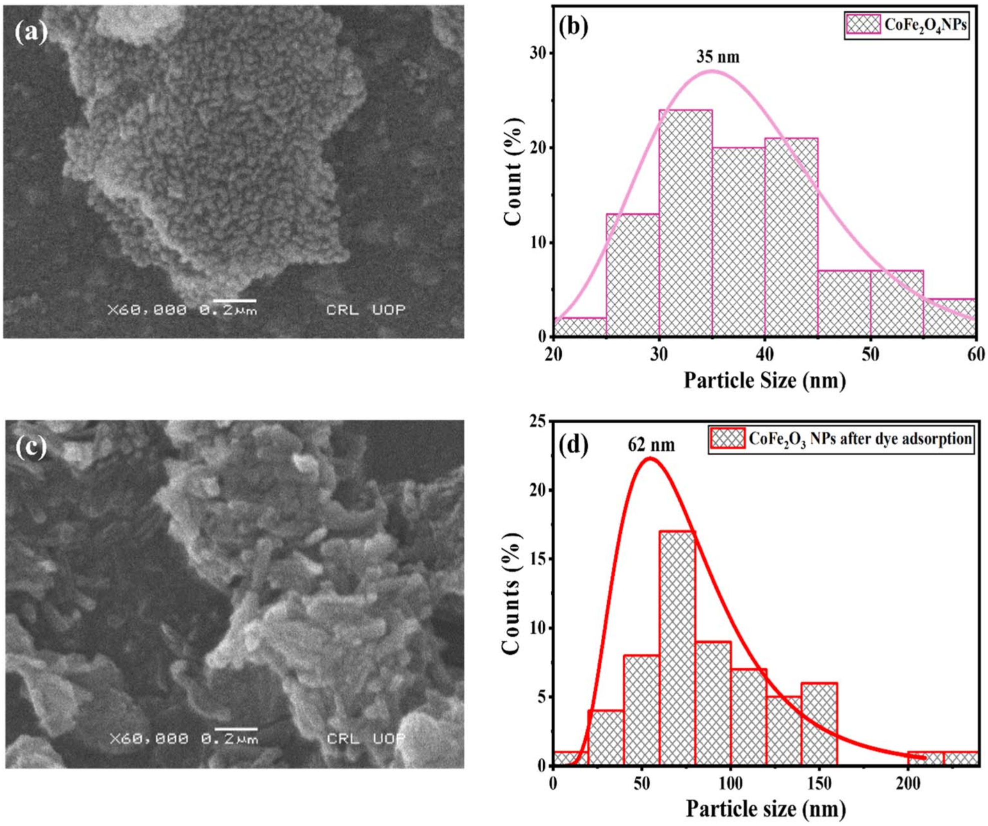

Fig. 4 Surface morphology and size analysis of $CoFe_2O_4$ NPs before and after RO16 dye adsorption: (a and c) SEM images before and after dye adsorption, (b and d) corresponding size distribution graphs.

was studied as shown in Fig. 5a to establish the best contact time between 0 and 120 min. The results showed that RO16 removal increases at the beginning of the process with an increase in contact time, reaching equilibrium at 60 min. The uptake of RO16 was observed to occur in two phases as a function of time. The first phase involved fast dye uptake during the first 20 min of adsorbate–adsorbent interactions, followed by a slow dye removal phase that lasted significantly longer (60 min) until equilibrium was reached. The higher % removal of RO16 dye at the start of the process could be owing to the abundance of active sites on the sorbent at this time. The % removal becomes less efficient during the slower phase as these sites are gradually occupied. Kumar and Gayathri reported that the adsorption efficiency of ZnO-NPs increases with contact time due to the availability of more active surface sites for dye binding, supporting our findings.[34] Fig. 5b findings indicate that the % removal of RO16 dye molecules decreases from 76 to 35% as the adsorbate concentration increases from 10 to 500 mg L^{-1}. This trend suggests that at lower concentrations, dye molecules have abundant adsorption sites on the $CoFe_2O_4$ NPs, enabling the effective removal of the dye from the solution. At higher RO16 concentrations, these molecules saturate the active binding sites of the NPs.[40] However, the adsorption capacity (q_e) increases because a higher concentration gradient enhances mass transfer, leading to greater dye uptake per unit mass of the adsorbent.[41] The effect of $CoFe_2O_4$ NPs dose was studied in the range of 0.25 to 2 mg mL^{-1} at solution pH, ambient temperature and initial concentration of 20 mg L^{-1} as shown in Fig. 5c. Results revealed that the RO16 dye removal increases from 49 to 90% with an incremental rise in the NPs dose from 0.25 to 2 mg mL^{-1}. This is due to increase in surface area and availability of greater number of free adsorption sites on surface of NPs.[35–37] Similar kinds of trends have been reported in literature for RO16 dye using TiO_2 nanocomposites[38] and cobalt ferrite NPs.[35] On other side adsorption capacity of NPs decreases from 39 to 8 mg g^{-1}. One possible explanation for this decrease in adsorption capacity with dose is the overlapping of active moieties, which reduces the surface area available for binding.[39]

Effect of temperature, surface charge, and pH. The effect of variable temperatures on the removal of RO16 by $CoFe_2O_4$ NPs was studied and displayed in Fig. 6a. The temperature was varied at 25, 30, 35, 40, and 45 °C, with a constant absorbent dose of 1 mg mL^{-1}, a constant solution pH, and a constant initial concentration of adsorbate (20 mg L^{-1}). The removal of RO16 dye onto the NPs was increased from 61.2 to 84.9% with rise in temperature from 25 to 45 °C because increasing temperature provide enough kinetic energy to RO16 dye molecules to undergo an interaction with surfaces sites at the surface of NPs.[40] Moreover, elevated temperatures can induce a swelling effect within the internal structure of the adsorbent, allowing deeper penetration of dye molecules. Two possible mechanisms

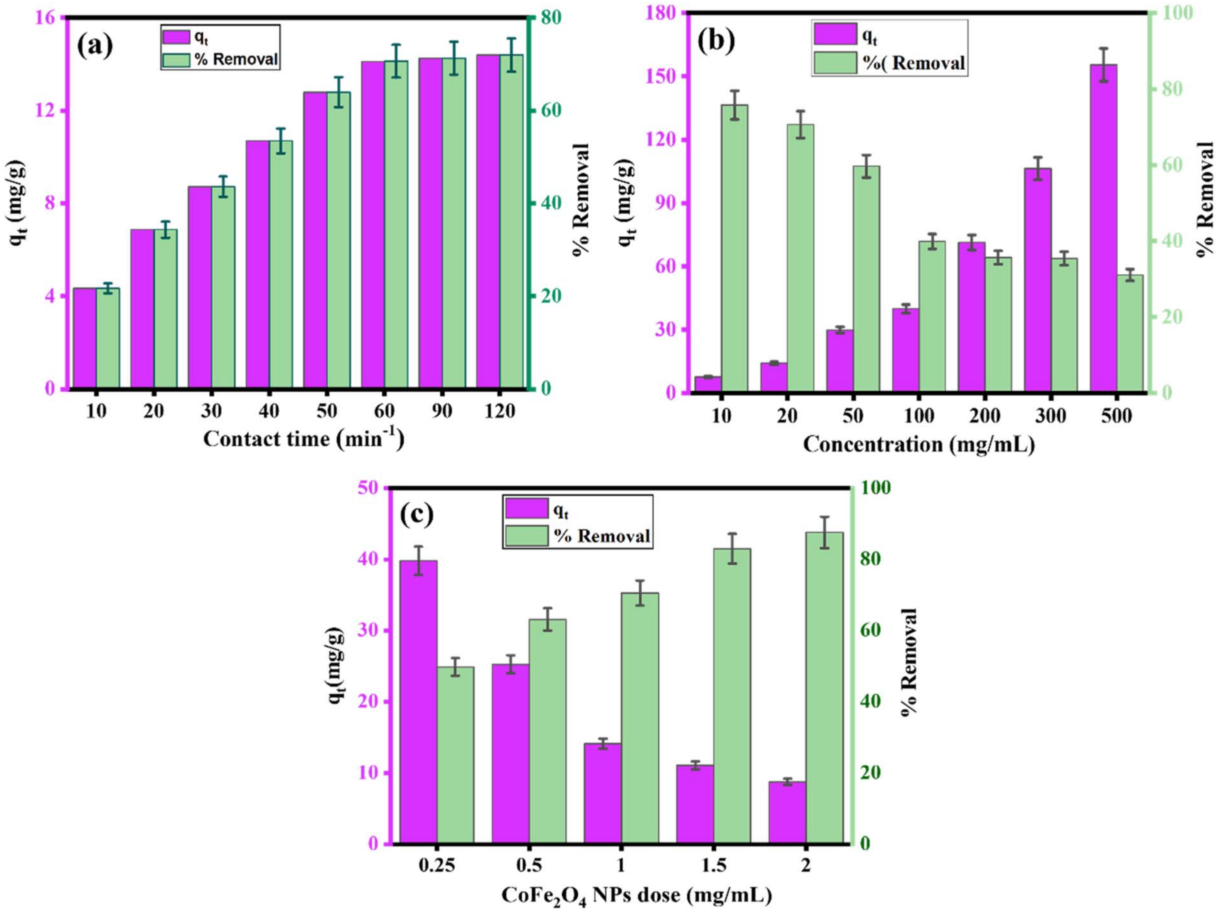

Fig. 5 Effect of experimental parameters on RO16 dye removal by $CoFe_2O_4$ NPs: (a) contact time (dose = 1 mg g^{-1}, $C_0 = 20$ mg L^{-1}, solution pH, $T = 298.15$ K), (b) effect of initial concentration (dose = 1 mg g^{-1}, solution pH, $T = 298.15$ K, contact time = 60 min), (c) effect of $CoFe_2O_4$ NPs (C_0 = 20 mg L^{-1}, solution H, T = 298.15 K, contact time = 60 min).

may explain this phenomenon: (i) expansion of the pore diameters of $CoFe_2O_4$ NPs, and (ii) breakage of internal bonds, such as hydrogen bonds between dye molecules and hydroxyl groups on the adsorbent surface, leading to the generation of additional active adsorption sites.[41] pH of the solution directly impacts the surface charge of the adsorbent and the extent of ionization of the adsorbate molecules. The zeta potential analysis of $CoFe_2O_4$ NPs in Fig. 6b demonstrates that the surface charge is strongly influenced by the pH of the medium. The zeta potential gradually decreases from positive to negative values as pH increases, and the point of zero charge (PZC) was observed at pH $\approx$ 3.3. Below this pH, the NPs surface is positively charged, which promotes electrostatic attraction with anionic dye molecules. Above the PZC, the surface becomes negatively charged, resulting in increased electrostatic repulsion. This behavior correlates well with the pH-dependent dye removal results as shown in Fig. 6c where the highest removal efficiency was observed at pH 2, followed by a gradual decline as pH increased to 10. The enhanced adsorption at acidic pH is attributed to the strong electrostatic interaction between the positively charged $CoFe_2O_4$ surface and negatively charged dye anions. Similar pH-dependent trends have been reported in previous studies, supporting that electrostatic forces dominate the adsorption mechanism of anionic dyes onto metal oxide nanoadsorbents.[35]

Equilibrium adsorption isotherm models

The equilibrium isotherm represents the relationship between the amount of adsorbate adsorbed per unit mass of adsorbent (q_e) and the equilibrium concentration of the adsorbate in the liquid phase (C_e). For the design and optimization of an adsorption system for the removal of dye from an aqueous solution, equilibrium isothermal data are necessary. The data for RO16 dye on $CoFe_2O_4$ NPs was evaluated using Freundlich,[42] Redlich Peterson, Langmuir and Temkin isotherm models and the results of parameters and constants were calculated and shown in Table 1 while the corresponding figures are provided in the SI as Fig. S1. Results revealed that the adsorption of RO16 by $CoFe_2O_4$ NPs was better fit in order of Freundlich > Redlich Peterson > Langmuir > Temkin in view of correlation coefficient (R^2) as shown in Fig. S1a–d. K_F and $1/n$ were found to be 4.7 mg g^{-1} and 0.58, which shows favorability of $CoFe_2O_4$ NPs for RO16 adsorption. When $1/n$ equals 1, the adsorption is linear, and the concentration of dye particles has no effect on the two stages.[43] The Redlich–Peterson model exhibited good fit to the

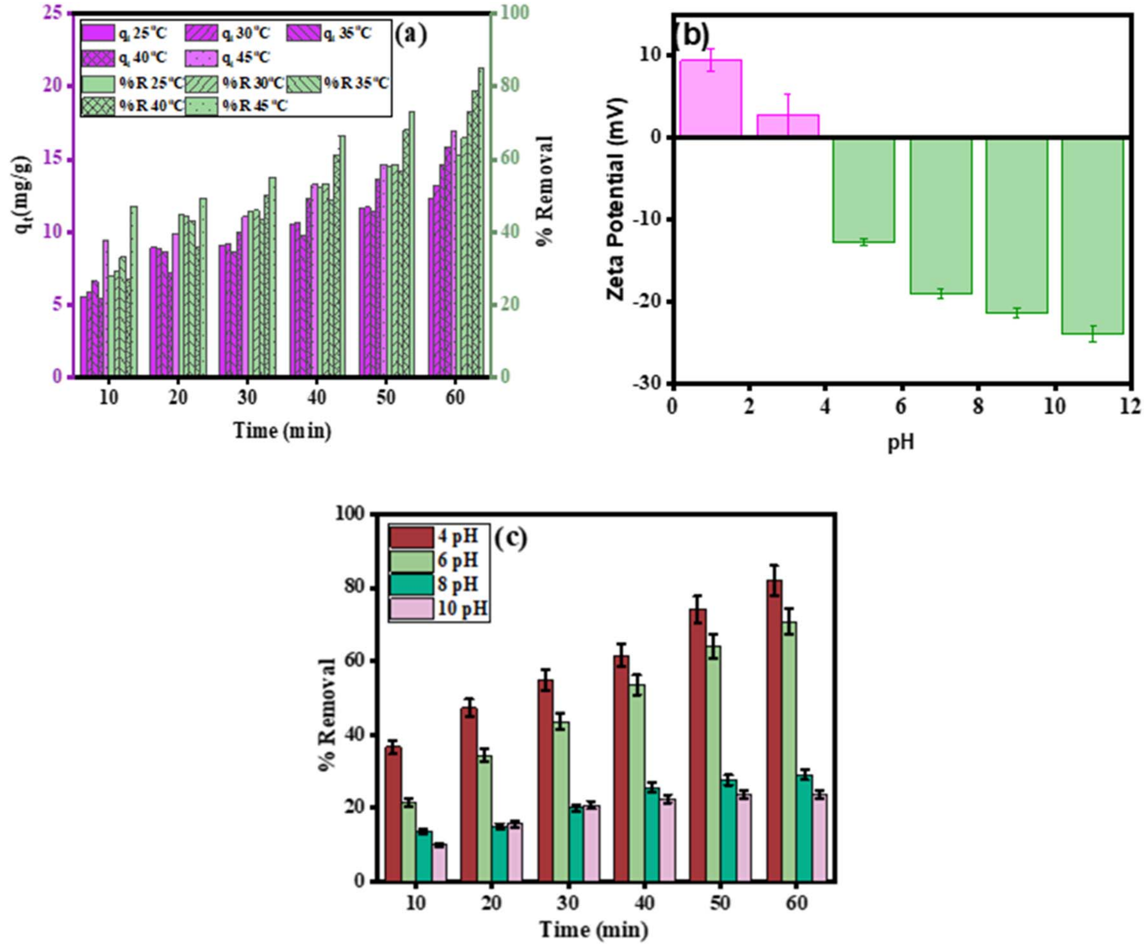

Fig. 6 (a) Effect of temperature (dose = 1 mg g^{-1}, C_0 = 20 mg L^{-1}, solution pH, contact time = 60 min), (b) pH influence on nanoparticle surface charge, (c) effect of different pH (dose = 1 mg g^{-1}, C_0 = 20 mg L^{-1}, T = 298.15 K, contact time = 60 min).

Table 1 Values of various adsorption parameters and error function for the removal of RO16 dye by $CoFe_2O_4$ NPs

Isotherms	Parameters	Values	EABS	χ^2	APE	Hybrid
Freundlich	K_f (mg g^{-1}) (L mg^{-1})$^{1/n}$	4.7	30.42	2.69	7.39	11.09
	$1/n$	0.58				
	R^2	0.995				
Redlich–Peterson model	K_R (L mg^{-1})	4.8	27.15	5.13	17.50	34.99
	g	0.4				
	R^2	0.994				
Langmuir	q_{exp} (mg g^{-1})	71.0	119.68	49.98	20.16	30.24
	q_{max} (mg g^{-1})	84.0				
	K_a (L mg^{-1})	0.03				
	R_L	0.2				
	R^2	0.985				
Temkin	B (mg g^{-1})	746.1	1028.10	267.98	401.97	68.25
	$B = RT/b_T$ (mg g^{-1})	26.8				
	$\ln(A_T)$	1.22				
	A_T (L mg^{-1})	3.38				
	R^2	0.866				

experimental data, with a high correlation coefficient (R^2 = 0.990). The calculated model parameters were K_R equal to 4.8 and g is equal to 0.4. g reflects the deviation from ideal monolayer adsorption predicted by the Langmuir isotherm, where $g = 1$ indicates Langmuir-type behavior and $g = 0$ corresponds to Henry's law. Values of g between 0 and 1 suggest heterogeneous adsorption similar to the Freundlich isotherm.[44] The obtained g value of 0.4 lies well within this range, indicating that the adsorption process follows Freundlich-type behavior, consistent with multilayer adsorption on a heterogeneous surface. The results obtained using the Langmuir isotherm showed correlation coefficient $R^2 = 0.985$. In addition, Langmuir constant (K_a), which is related to the heat of adsorption, was found to be 0.03. The dimensionless separation factor (R_L), used to predict the affinity between the adsorbate and the adsorbent using Langmuir parameters was 0.20 which shows adsorption of RO16 was favorable. Temkin model with R^2 value of 0.866 is less fit among all these models. A similar fitting result was obtained for the various adsorbent–pollutant systems.[42,45,46]

Equilibrium kinetics and thermodynamic analysis. The adsorption kinetics of RO16 dye removal employing $CoFe_2O_4$ NPs were investigated. The plots of PFO, PSO and IPD kinetic models are presented in SI in Fig. S2 and the respective parameters and constant are listed in Table 2. The PFO model showed relatively good fitting at lower concentrations $R^2 = 0.997$ but deviated at higher concentrations due to the difference between experimental and calculated adsorption capacities. The PSO model generally provided a better description of the adsorption kinetics at intermediate concentrations (50 and 100 mg L^{-1}), $R^2 = 0.997$ and 0.995, respectively, suggesting that chemisorption involving electron sharing or exchange may govern the adsorption process. The intraparticle diffusion model exhibited multi-linearity, indicating that adsorption was controlled by more than one step. At higher concentrations, the intercept I increased significantly, suggesting a greater contribution of boundary layer diffusion along with intraparticle diffusion in controlling the rate of adsorption. Overall, the kinetic study suggests that the adsorption of RO16 onto $CoFe_2O_4$ NPs proceeds mainly through a pseudo-second-order mechanism, with both surface adsorption and intraparticle diffusion playing significant roles in the overall process.

The thermodynamic parameters including change in enthalpy (ΔH) and entropy (ΔS) were computed from van't Hoff plot for RO16 removal by $CoFe_2O_4$ NPs with rise in temperature at equilibrium time, *i.e.*, 60 min, shown in Fig. S2d (SI). The values of all parameters are given in Table 3. The positive sign of ΔH (51 kJ mol^{-1}) confirms that the adsorption process is endothermic in nature.[47] Since this enthalpy change lies in the intermediate range as commonly shown by physisorption, it infers that the interaction between the adsorbent and the dye molecules is mostly physical in nature and not chemical. A study shows that if ΔH value less than 80 kJ mol^{-1} then it is physisorption and greater the 80 kJ mol^{-1} is chemisorption.[48] Additionally, the positive sign of ΔS indicates an increase in the randomness or disorder at the solid solution interface during the process of adsorption. The distribution coefficient (K_d) increased with temperature, indicating enhanced adsorption capacity at elevated temperatures.

Error function to find most appropriate isotherm model. The adsorption equilibrium data were fitted to four isotherm models Freundlich, Langmuir, Temkin and Redlich–Peterson, and their suitability was assessed using statistical error functions absolute error (EABS), chi-square (χ^2), average percentage error (APE), and hybrid error function (HYBRID) and values are given in Table 1. Among the tested models, the Redlich–Peterson model exhibited the lowest EABS (27.15) along with a low χ^2 (5.13), indicating good agreement between calculated and experimental q_e values across the concentration range. The Freundlich model also provided a good fit, with low error values (EABS = 30.421, $\chi^2 = 2.69$, APE = 7.39%, HYBRID = 11.09%), suggesting heterogeneous surface adsorption with multilayer formation. In contrast, the Langmuir model showed relatively higher errors, particularly at high equilibrium concentrations. The Temkin and model produced the highest errors, indicating poor representation of the experimental data. Overall, the error analysis confirmed that the Redlich–Peterson and Freundlich models best described the adsorption behavior in the present system.

Photocatalytic degradation performance of $CoFe_2O_4$ nanoparticles. To further assess the multifunctional nature of $CoFe_2O_4$ NPs due to their semiconducting nature, their photocatalytic degradation activity toward RO16 dye under visible light irradiation was evaluated. Thus, $CoFe_2O_4$ NPs shows dual functionality, where it first adsorbs the RO16 dye molecules and then effectively degrades them under light irradiation.

Table 2 Parameters and constants of PFO, PSO, and IPD kinetic models' fitness

		Initial reactive orange 16 dye concentration (mg L^{-1})				
Kinetic models	Parameters	10 mg L^{-1}	20 mg L^{-1}	50 mg L^{-1}	100 mg L^{-1}	300 mg L^{-1}
PFO	$q_{e\ exp}$ (mg g^{-1})	7.58	14.12	29.83	39.91	106.34
	$q_{e\ cal}$ (mg g^{-1})	7.24	15.84	28.84	28.18	95.49
	K_1 (min^{-1})	0.00	0.04	0.06	0.06	0.00
	R^2	0.997	0.940	0.990	0.929	0.984
PSO	$q_{e\ exp}$ (mg g^{-1})	7.58	14.12	29.83	39.91	106.34
	$q_{e\ cal}$ (mg g^{-1})	11.47	26.89	37.86	36.63	149.92
	K_2 (g (mg^{-1} min^{-1}))	2×10^{-3}	7×10^{-4}	1×10^{-3}	4×10^{-3}	2×10^{-3}
	R^2	0.964	0.955	0.997	0.995	0.890
IPD	I	2.03	2.70	14.10	25.40	28.80
	K_{diff} (mg g^{-1} $min^{-1/2}$)	0.18	0.39	0.58	0.50	2.42
	R^2	0.972	0.993	0.865	0.900	0.973

Table 3 Thermodynamic parameters for RO16 removal by $CoFe_2O_4$ NPs

	Temp. (K)	K_d	ΔG (kJ mol^{-1})	ΔS (J K^{-1} mol^{-1})	ΔH (kJ mol^{-1})	R^2
$CoFe_2O_4$ NPs	298.15	1.58	−8.60	0.20	51.0	0.984
	303.15	1.94	−9.60			
	308.15	2.72	−10.60			
	313.15	3.77	−11.50			
	318.15	5.66	−12.80			

Photocatalytic degradation of RO16 dye. The photocatalytic degradation efficiency of $CoFe_2O_4$ NPs was tested against RO16 dye. For this aqueous solution of RO16 dye with 100 mg L^{-1} concentration was treated with 1 mg mL^{-1} of $CoFe_2O_4$ NPs nanoparticles were added to the dye solution and stirred in visible light for 60 minutes, an aliquot of 5 mL was taken after 10 minutes and then subjected to centrifugation at 3000 rpm for 5 min. Dye solution after centrifugation was subjected to the UV-Vis spectral analysis to record the photo catalytic degradation of RO16 dye. Following eqn (3) was used to calculate the photocatalytic degradation of RO16 dye.

$$\text{Degradation}(\%) = \left(\frac{C_0 - C_t}{C_0}\right) \times 100 \tag{3}$$

Optimization studies for RO16 dye degradation by $CoFe_2O_4$ NPs

Effect of pH. The pH of the solution is an important parameter governing the nanoparticle dye interaction, followed by its overall photocatalytic degradation efficiency.[49] Fig. 7 presents time-dependent UV-Visible spectra (a–c) and final photocatalytic degradation efficiencies (d) under acidic (pH 2), neutral (pH 6.5), and alkaline (pH 12) conditions. The spectra (a–c) show a main absorption band around 490–500 nm, characteristic of the RO16 dye's azo (–N═N–) chromophore and π-conjugated structure. Upon exposure to visible light, a rapid and continuous decrease in the intensity of this band is observed across all experiments, providing direct kinetic evidence of chromophore cleavage and dye mineralization. The highest degradation rate was observed under highly acidic conditions (pH 2, Fig. 7a), due to favorable electrostatic interaction at given pH. NPs are positively charged in the acidic medium, enabling promising interaction with the anionic dye due to negatively charged sulfonate groups. At this pH, the λ_{max} showed an immediate shift and the absorbance dropped quickly, indicating rapid structural changes and subsequent cleavage of the azo bond. Conversely, the photocatalytic degradation efficiency was considerably slower under pH 6.5 (Fig. 7b) and alkaline pH 12 in (Fig. 7c), which can be attributed to the lower interaction of anionic dye with negatively charged surface NPs at given pH. Acidic medium also favors the RO16 molecules to undergo protonation, alter its molecular configuration and make the azo bond more vulnerable to nucleophilic attack by reactive oxygen species. Fig. 7d demonstrates the overall degradation efficiency of RO16, in various pH, with a maximum degradation efficiency of 83.5% was achieved at pH 2 after 60 minutes of irradiation. This efficiency sharply declined to 33.5% at pH 6.5 and further to 21% in the highly alkaline medium of pH 12. This clear trend suggests a strong pH-dependent mechanism. It is noteworthy that, like pH-dependent behavior, the photocatalyst dose also governs the availability of surface-active sites and the generation of reactive species, thereby directly influencing the overall photocatalytic degradation efficiency of RO16 under visible light irradiation.

Effect of photocatalyst dose. Fig. 8a and b displays the time-dependent UV-Visible absorption spectra of RO16 solution at photocatalyst doses of 0.5 g L^{-1} and 1.5 g L^{-1}, respectively. A steady decline in the intensity of the absorption band centered near 490–500 nm confirms the progressive degradation of the dye upon exposure to light irradiation. Bar graph in Fig. 8c summarizes the overall photocatalytic degradation efficiency, which increased from 30.4% at 0.5 g L^{-1} to 33.5% at 1.0 g L^{-1} and reached 38.8% at 1.5 g L^{-1}. An 8% increase in dye degradation was observed, indicating that photocatalyst loading has a minor effect. The slight enhancement arises from more active sites and improved photon absorption, generating additional reactive oxygen species. Similar results are provided in the literature, which supports our findings.[50]

Effect of initial RO16 concentration and PFO kinetic model. Fig. 9a shows the photocatalytic performance of $CoFe_2O_4$ NPs for various initial RO16 concentrations (10, 20, 50, 100, 200, 300, 400, and 500 mg L^{-1}) at a fixed dose of 1 mg mL^{-1} and neutral solution pH (6.5). A given number of NPs were added to each dye solution, stirred for 60 minutes under visible light. The highest photocatalytic degradation efficiency was observed at a lower dye concentration of 96% for 10 mg L^{-1}. The degradation efficiency decreases continuously with initial RO16 concentration and reaches 13% for 500 mg L^{-1} dye concentration (Fig. 9b). Such a decrease in photocatalytic degradation efficiency of NPs can be attributed to the blockage of the photocatalyst active sites.[50,51] Fig. 9b shows a decrease in overall degradation efficiency from 96% at 10 mg L^{-1} to 13% at 500 mg L^{-1} after 60 minutes of irradiation. Fig. 9c, shows the photocatalytic degradation mechanism follows pseudo-first-order kinetics, confirmed by the linear relationship between $\ln(C_0/C_t)$ and irradiation time. The corresponding kinetic parameters are summarized in Table 4. The apparent rate constant (K_{app}) values plotted in Fig. 9d show a decreasing reaction rate with increasing dye concentration, emphasizing that higher dye loads result in significant light attenuation and

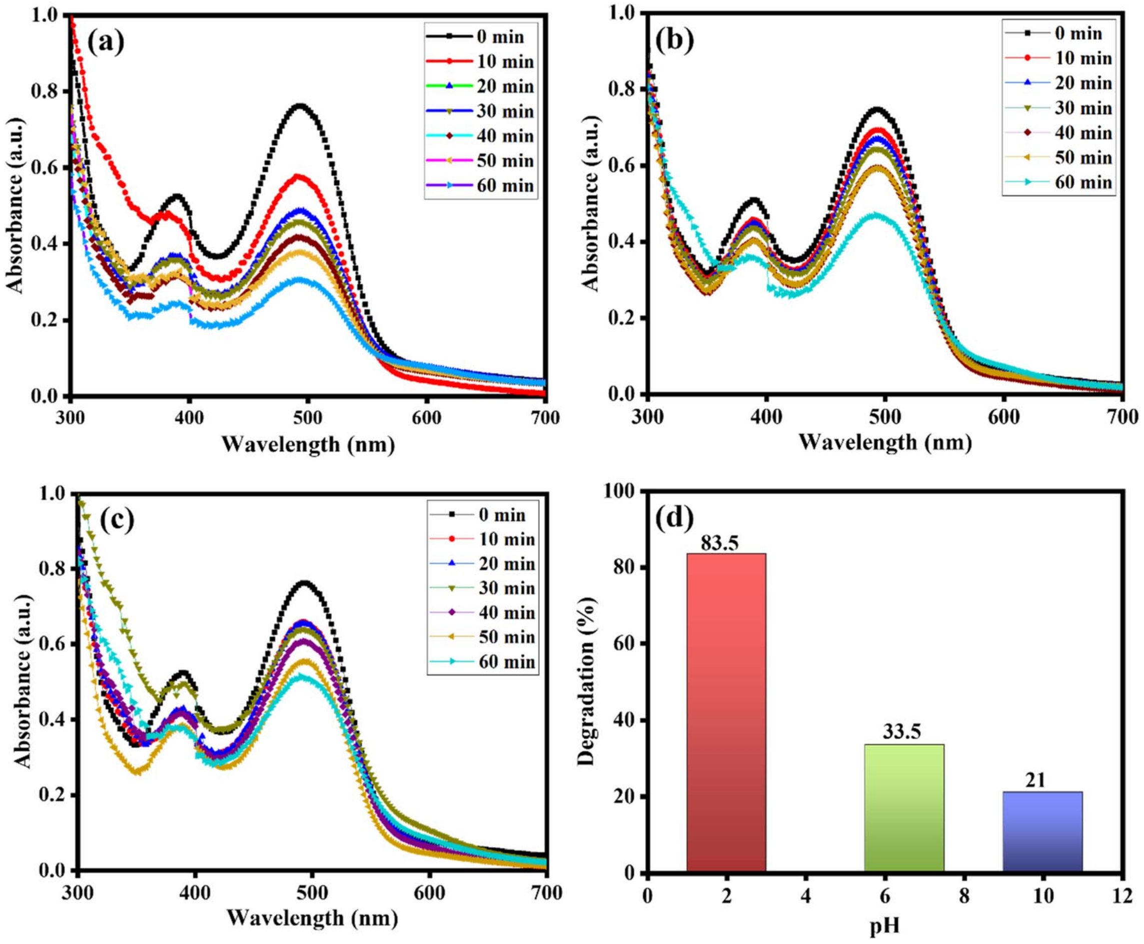

Fig. 7 UV-Visible spectra of RO16, before and after light irradiation at various pH. (a) pH 2, (b) pH 6.5, (c) pH 12, and (d) percent degradation ($C_0 = 100$ mg L^{-1}, dose = 1 mg mL^{-1}, volume = 50 mL, $T = 298.15$ K, time = 60 min).

lower generation of reactive species, thus slowing the overall photocatalytic degradation rate.

Adsorption and photocatalytic degradation mechanism

The degradation of RO16 dye by $CoFe_2O_4$ NPs involves a synergistic adsorption–photocatalysis mechanism. The effectiveness of an adsorption system is fundamentally tied to the physicochemical interactions between the adsorbate and the adsorbent. A comprehensive understanding of these interactions is crucial for elucidating the underlying adsorption mechanism. When pollutants are adsorbed onto ferrites, a variety of interactions are involved, including hydrogen bonding, π–π interactions, surface complexation, electrostatic interactions, chemisorption, and ion exchange in an aqueous medium. Metal oxides, such as $CoFe_2O_4$, develop a layer of surface hydroxyl groups (–OH) through the reaction of water molecules with the material's surface.

The adsorption of RO16 dye onto the $CoFe_2O_4$ NPs is driven by a complex interplay of these interactions, as shown in Fig. 10a. A predominant electrostatic attraction occurs between the negatively charged RO16 dye anions and the positively charged surface of the $CoFe_2O_4$ NPs. In addition to electrostatic forces, the adsorption mechanism involves H-bonding interactions between the surface hydroxyl groups of the NPs and the aromatic rings of the RO16 dye. Furthermore, the π–π interactions between the N═N azo group and the aromatic rings of the RO16 dye with the d-orbitals of the NPs also contribute significantly to the adsorption process. This intricate combination of electrostatic, hydrogen-bonding, and π–π interactions governs the adsorption of RO16 dye, underscoring the efficacy of $CoFe_2O_4$ NPs for dye removal. This adsorption step enhances the local concentration of dye near the active sites, facilitating efficient charge transfer during photocatalysis. Upon exposure to visible light, as shown in Fig. 10b, the energy absorbed by the material that excites electrons (e^-) from the valence band (VB) to the conduction band (CB) of the nanomaterial, which possesses a narrow band gap ($E_g = 2.91$ eV) calculated from the Tauc equation mentioned in eqn (6). This charge separation generates reactive positive holes (h^+) in the valence band. The photogenerated charge carriers then initiate the degradation *via* redox reactions.[52] The electrons in the conduction band, which have a potential of −0.15 eV *vs.* NHE, react with dissolved molecular oxygen (O_2) to produce the superoxide radical anion (O_2^-), a potent oxidizing species, as shown in eqn (4).

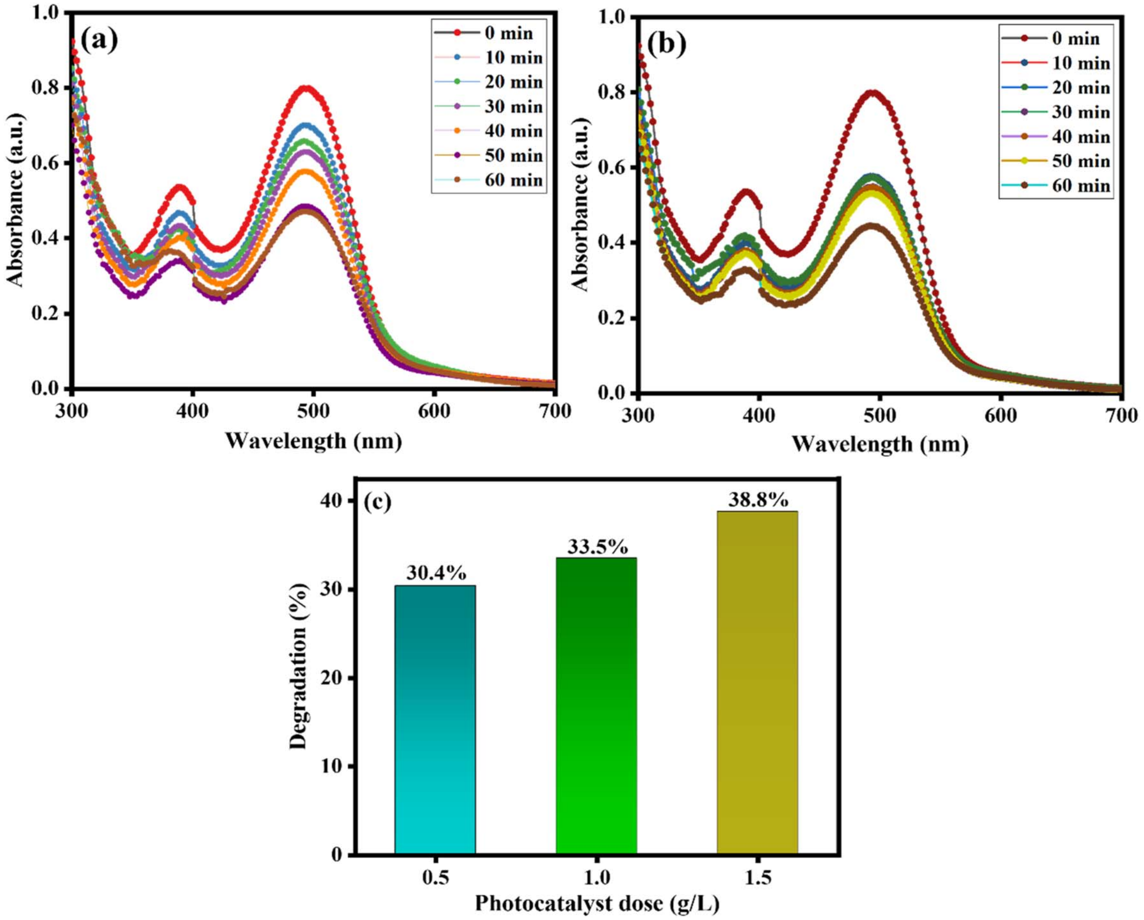

Fig. 8 UV-Visible spectra of RO16, dose effect (a) dose (0.5 g L^{-1}), (b) dose (1 g L^{-1}), and (c) percent degradation ($C_0 = 100$ mg L^{-1}, volume = 50 mL, $T = 298.15$ K, time = 60 min).

$$e_{CB}^{-} + O_2 \rightarrow \cdot O_2^{-} \tag{4}$$

The holes in the valence band, with a potential of 2.76 eV *vs.* NHE, react with water (H_2O) to generate the hydroxyl radical (OH), as shown in eqn (5). The OH radical is the primary, non-selective oxidant responsible for attacking the RO16 dye molecule.

$$h_{VB}^{+} + H_2O \rightarrow \cdot OH + H^{+} \tag{5}$$

$$(\alpha\hbar\nu)^n = A(\hbar\nu - E_g) \tag{6}$$

Collectively, the OH and O_2^{-} radicals rapidly attack the RO16 molecule, leading to the efficient cleavage of the azo chromophore, the formation of degraded intermediate products, and ultimately, complete mineralization into carbon dioxide (CO_2), water (H_2O), and mineral acids. The relative ease of charge transfer and radical generation confirms the suitability of the $CoFe_2O_4$ photocatalyst for visible-light-driven degradation applications. Adsorption process localizes dye molecules at the photocatalyst surface, while photocatalysis promotes their oxidative degradation, confirming the high efficiency of $CoFe_2O_4$ NPs for visible-light-driven dye removal.

Scavenging studies

Fig. 10c illustrates the influence of different scavengers at varying concentrations (0.01 and 0.02 M) on the photocatalytic degradation of RO16 dye using cobalt ferrite nanoparticles. In the presence of *n*-propanol ($^{\cdot}$OH scavenger), the degradation efficiency significantly decreased to 63.1% (0.01 M) and 47.5% (0.02 M), indicating the major role of hydroxyl radicals.[53] For $AgNO_3$ (electron scavenger), only a slight change was observed, with efficiencies of 81.9% (0.01 M) and 88.1% (0.02 M). Such a slight increase in degradation efficiency at higher $AgNO_3$ concentration could be attributed to the involvement of silver metal in photocatalytic activity.[54] In contrast, EDTA (hole scavenger) reduced the degradation efficiency from 85% to 69.4% at 0.01 M and 0.02 M, respectively.[55] These results confirm that the degradation of RO16 dye primarily involves reactive species generated by cobalt ferrite nanoparticles, particularly $\cdot$OH radicals and photogenerated holes.

The band energy position of cobalt ferrite nanoparticles was calculated using Mulliken electronegativity theory, as shown in eqn (7) and (8).[55]

$$E_{VB} = X - 0.5E_g \tag{7}$$

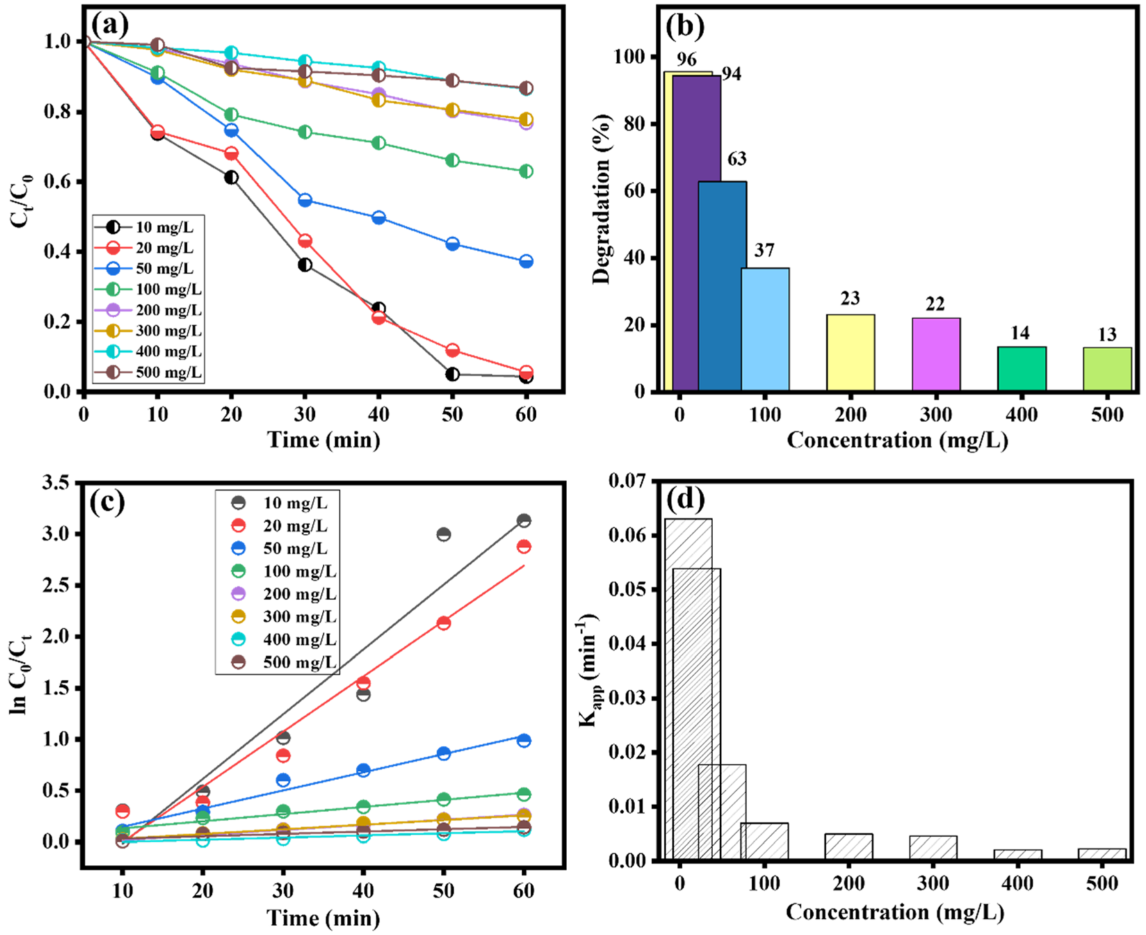

Fig. 9 UV-Visible spectra of RO16. (a) Concentration effect (b) percent degradation, (c) PFO, and (d) K_{app} *vs.* time (min) (dose = 1 mg mL^{-1}, solution pH, volume = 50 mL, T = 298.15 K, time = 60 min).

Table 4 Pseudo-first-order kinetic parameters for RO16 degradation by $CoFe_2O_4$ nanoparticles

C_0 (mg L^{-1})	K_1 (min^{-1})	R^2
10	0.063	0.9
20	0.053	0.951
50	0.017	0.966
100	0.006	0.95
200	0.004	0.998
300	0.004	0.985
400	0.002	0.916
500	0.002	0.85

$$E_{CB} = E_{VB} - E_g \tag{8}$$

where X is the absolute electronegativity, E_g is the band gap energy, and E_c represents the energy of the conduction band (a constant value of 4.5 eV on the hydrogen scale). The calculated conduction and valence band positions of cobalt ferrite nanoparticles were −0.155 and 2.76 eV, respectively.

AI-based model and interpretation of adsorption parameters

To complement the experimental adsorption study, AI-based models were employed to evaluate the relative importance, interactions, and correlations among operational parameters affecting RO16 dye removal by $CoFe_2O_4$ NPs. These approaches provided additional predictive insights beyond conventional kinetic and isotherm analyses. The SHapely Additive explanation (SHAP) summary plot (Fig. 11a) revealed that contact time had the greatest influence on dye removal, followed by initial concentration, pH, and adsorbent dose, while temperature contributed comparatively less. This ranking is consistent with batch adsorption experiments, where equilibrium time and concentration critically governed removal efficiency. The SHAP beeswarm plot (Fig. 11b) further illustrated that longer contact times and higher adsorbent doses enhanced removal efficiency, whereas alkaline pH values reduced adsorption, in agreement with experimental findings that acidic conditions favor dye uptake. The principal component analysis (PCA) in Fig. 11c showed clear clustering of experimental conditions, with high-removal cases grouping, confirming that low pH, longer contact times, and moderate concentrations dominate adsorption efficiency. Meanwhile, the correlation heatmap (Fig. 11d)

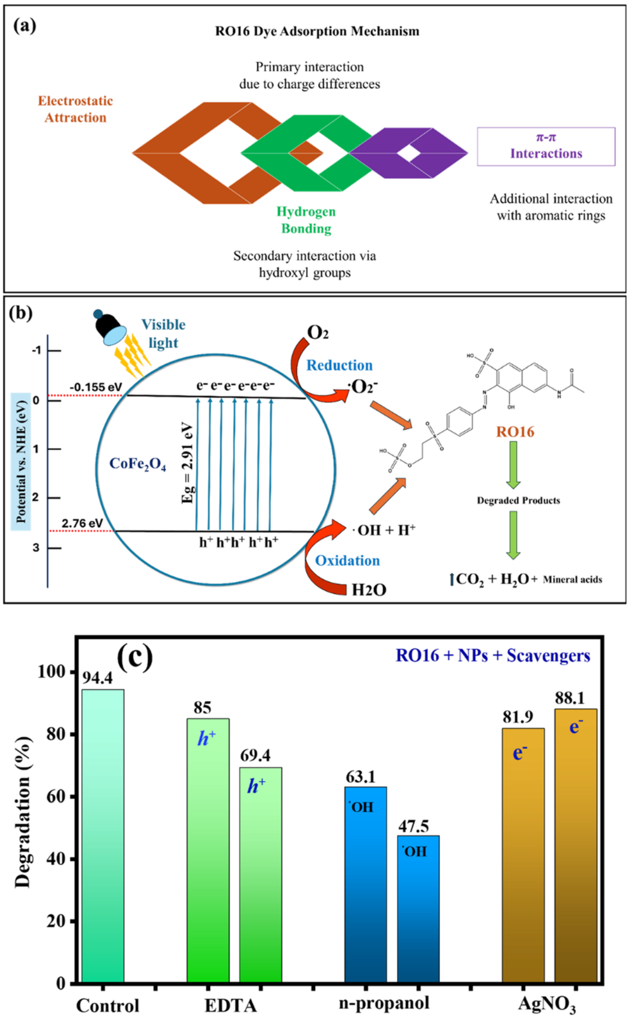

Fig. 10 (a) Adsorption and (b) photocatalytic degradation mechanisms by the $CoFe_2O_4$ NPs, (c) effect of h^+, $\cdot OH$, and e^- radical scavengers (0.01 M and 0.02 M) on the photocatalytic degradation of RO16 using $CoFe_2O_4$ NPs (dose = 1 mg mL^{-1}, $C_0 = 20$ mg L^{-1}, solution pH, volume = 30 mL, $T = 298.15$ K, time = 60 min).

demonstrated that contact time ($r = 0.52$) and adsorbent dose ($r = 0.24$) correlated positively with % removal, while pH ($r = -0.41$) and initial concentration ($r = -0.43$) correlated negatively.

Tomato seed germination and antibacterial study of $CoFe_2O_4$ NPs. The toxicity study, as shown in Fig. S3a (SI), indicated that the tomato seed germination rate was higher than 90% in both the control and $CoFe_2O_4$ NPs alone groups, which implies that $CoFe_2O_4$ NPs are safe for seeds. In the NPs treated group, germination was reduced to 71%, indicating minor residual effects following dye adsorption but retaining acceptable seed viability. Conversely, seeds treated with RO16 dye alone had a significant reduction to 32%, verifying the intense phytotoxicity of the dye. In general, $CoFe_2O_4$ NPs were safe and efficient in lowering dye toxicity in water. The findings of this study are consistent with previously reported results, where exposure to various NPs showed minimal or no inhibitory effects on tomato seed germination. Similar to the observations of Song *et al.* (2013).[56] The $CoFe_2O_4$ NPs used in the present work did not cause any significant reduction in germination percentage. This agreement further supports that certain metal oxide NPs, including $CoFe_2O_4$ NPs, exhibit low phytotoxicity and can be considered environmentally safe for practical applications such as wastewater treatment.[57]

While in the antibacterial study, as depicted in Fig. S3b, no visible zone of inhibition was observed around the wells containing $CoFe_2O_4$ NPs, indicating no antibacterial activity[58] under the tested conditions. In contrast, the positive control (kanamycin, 1 mg mL^{-1}) exhibited clear zones of inhibition measuring approximately 0.7 cm, 1.0 cm, and 1.2 cm in diameter. The synthesized $CoFe_2O_4$ NPs did not exhibit any observable antibacterial activity against *Pseudomonas aeruginosa* PAO1 as determined by the agar well diffusion method. The absence of a clear inhibition zone may be attributed to several factors, including insufficient diffusion of NPs in the agar medium, nanoparticle aggregation, or low intrinsic antibacterial properties of the tested ferrite compositions. *P. aeruginosa* is a Gram-negative bacterium known for its robust outer membrane, which may hinder the interaction of NPs with cellular targets. In contrast, the positive control (kanamycin) showed clear antibacterial activity, validating the assay. Our findings parallel those of Sulaiman *et al.* (2021), who reported no observable antibacterial activity of pure $CoFe_2O_4$ NPs (sintered at 400 °C and 600 °C) against *Enterococcus faecium* using the Kirby–Bauer method, unless the NPs were combined with chlorhexidine.[59] This supports our results and suggests that the absence of activity may be due to both poor diffusion in agar and the low intrinsic antimicrobial potential of ferrite NPs at 1 mg mL^{-1}.

Desorption efficiency of $CoFe_2O_4$ NPs. A major characteristic of an adsorbent is its capability to be regenerated and reused in multiple desorption cycles. These factors considerably impact the overall performance and cost of the adsorption process.[60] In this study, the regeneration data are provided in the SI (Fig. S4), and 0.1 M NaOH was employed as the desorbing agent to assess the reusability of $CoFe_2O_4$ nanoparticles. Initially, 50 mg of the $CoFe_2O_4$ nanoparticles were dispersed in 50 mL of RO16 dye solution (20 mg L^{-1}). The suspension was stirred at 200 rpm on an orbital shaker for 60 minutes to ensure maximum adsorption. Following this, the dye-laden NPs were collected by centrifugation and thoroughly rinsed with distilled water to remove any loosely bound dye molecules. For the desorption step, the used nanoparticles were immersed in 50 mL of 0.1 M NaOH and agitated for another 60 minutes to facilitate dye desorption. Afterward, the NaOH containing the released dye was decanted, and the nanoparticles were once again washed with distilled water to eliminate NaOH residues. The cleaned particles were then dried at 60 °C for 1 hour to prepare them for reuse. This process was repeated for up to five cycles using the same batch of nanoparticles, allowing assessment of their stability and regeneration potential over multiple uses. During this % removal decrease from 90% to 72% after five cycles. So, it can be said that the material is a useful adsorbent for treating dye contaminated water.

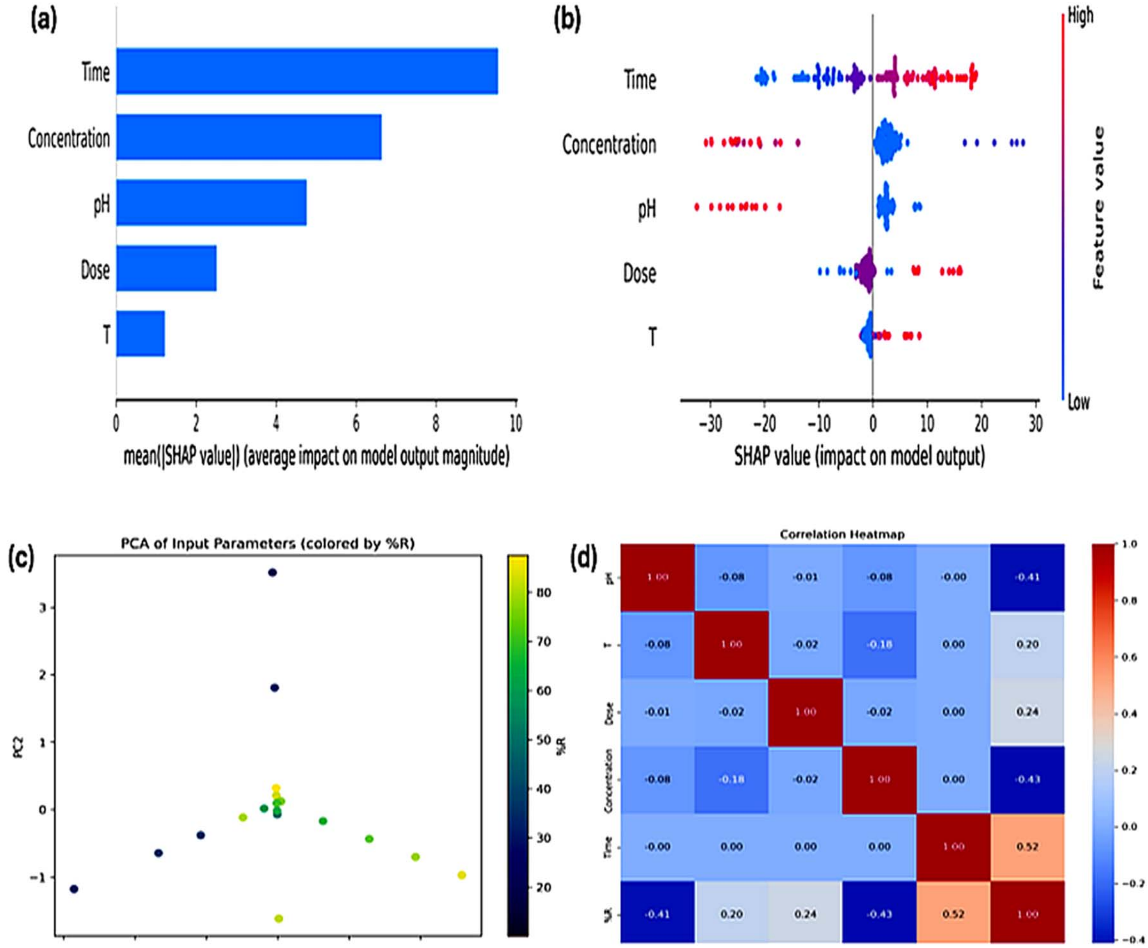

Fig. 11 AI-based analysis of RO16 dye removal by $CoFe_2O_4$ NPs: (a) SHAP summary, (b) SHAP beeswarm, (c) PCA clustering, and (d) correlation heatmap of parameters with % removal.

Conclusion

This study developed $CoFe_2O_4$ NPs through a simple co-precipitation method and demonstrated their remarkable efficiency for the removal of RO16 dye *via* an integrated adsorption–photocatalysis mechanism. Structural and optical analyses confirmed the formation of a mesoporous spinel nanomaterial with an optimal band gap for visible-light activation. The adsorption data followed the Freundlich and Redlich–Peterson isotherms, while pseudo-second-order kinetics suggested chemisorption involvement. Thermodynamic parameters confirmed the endothermic and spontaneous nature of adsorption. Under visible light, the NPs achieved rapid photocatalytic degradation through the generation of hydroxyl and superoxide radicals, enabling efficient dye breakdown. AI-assisted data analysis provided predictive insights, validating experimental observations and ranking key parameters influencing the adsorption efficiency. The eco-safety assessment confirmed that the NPs exhibit negligible phytotoxic or cytotoxic effects, supporting their environmental compatibility. Collectively, these findings establish $CoFe_2O_4$ NPs as a highly active, stable, and environmentally sustainable nanomaterial capable of uniting adsorption and photocatalysis for effective treatment of dye-contaminated wastewater.

Author contributions

Nasira Hussain: benchwork, characterization, and initial draft preparation. Muhammad Younas Afzal and Shanza Shafaat: bench work and characterization. Bilal Ahmad Zafar Amin and Faheem Shah: funding. Muhammad Bilal and Ahson Jabbar Shaikh: conceptualization, visualization, methodology, investigation, supervision, writing, reviewing, editing, and validation. All authors read and approved of the final manuscript.

Conflicts of interest

The authors declare that they have no competing interests.

Data availability

All data generated or analyzed during this study are included in this published article (see the figures). Additional data is provided in the supplementary information (SI) of this article.

Raw data supporting the findings of this study are available from the corresponding author upon reasonable request. Supplementary information: the details of adsorption isotherms including Freundlich model, Langmuir model, Temkin isotherm model, and Redlich–Peterson isotherm model; error function test details; kinetic models including pseudo 1st order kinetics, pseudo-second order kinetics, intra-particle diffusion model, and thermodynamics of adsorption. SI also includes figures of equilibrium adsorption isotherm models, equilibrium kinetics, thermodynamics analysis, tomato seed germination, antibacterial study of $CoFe_2O_4$ nanoparticles, and desorption efficiency of $CoFe_2O_4$ nanoparticles. See DOI: https://doi.org/10.1039/d6ra02108e.

Acknowledgements

This work was supported by the Deanship of Scientific Research, Vice Presidency for Graduate Studies and Scientific Research, King Faisal University, Saudi Arabia [Grant No. KFU261932]. Artificial intelligence tools, including ChatGPT (OpenAI), were used to support this work specifically for language refinement, grammar correction, and improving the clarity of text. All scientific ideas, experimental work, data interpretation, results, and conclusions presented in the manuscript are the authors' own. The authors carefully reviewed, edited, and verified all AI-assisted content to ensure accuracy and originality. The authors take full responsibility for the content of the published article.

References

1 Y. Yu, C. Duan, S. Li, C. Peng, J. Yang, K. Yan, *et al.*, Relationship between environmental pollution and economic development in late-developing regions shows an inverted V, *Sci. Total Environ.*, 2022, **838**, 156295.

2 S. H. Hashemi and M. Kaykhaii, Azo dyes: sources, occurrence, toxicity, sampling, analysis, and their removal methods, *Emerging Freshwater Pollutants*, Elsevier, 2022, pp. 267–287.

3 A. Negi, Environmental impact of textile materials: challenges in fiber–dye chemistry and implication of microbial biodegradation, *Polymers*, 2025, **17**(7), 871.

4 F. Ruscasso, I. Cavello, M. Butler, E. L. Loveira, G. Curutchet and S. Cavalitto, Biodegradation and detoxification of reactive orange 16 by Candida sake 41E, *Bioresour. Technol. Rep.*, 2021, **15**, 100726.

5 M. Khatri, R. A. Al-Juboori, M. Mehdi, N. K. Khanzada and N. Hilal, Adsorption Techniques for Dye Removal/Recovery from Industrial Wastewater, *Water Treatment*, CRC Press, 2025, pp. 82–108.

6 M. Islam, Z. U. H. Khan, A. Islam, S. Khasim, F. Ahmad, N. Ahmad, *et al.*, Smart adsorbent frameworks enabling high-efficiency pharmaceutical degradation via adsorption, *RSC Adv.*, 2026, **16**(16), 14688–14727.

7 M. Hussain, A. Riaz, H. Zeb, A. Ali, R. Mujahid, F. Ahmad, *et al.*, Paving the path to water security: The role of advanced adsorbents in wastewater treatment, *J. Water Proc. Eng.*, 2025, **71**, 107333.

8 M. Batool, A. Mehmood, S. Arif, M. Jalal, F. Ahmad and M. Waseem, Novel and recyclable $Ca(OH)_2$ and $Mg(OH)_2$ modified amberlyst-15 for selective removal of heavy metal ions, *Process Saf. Environ. Prot.*, 2025, **199**, 107246.

9 A. Alam, F. Fadhillah, J. Ahmad, F. Ahmad, F. A. A. Ali, M. U. H. Shah, *et al.*, Cadmium removal from water using conventional and emerging adsorbents: Current status, challenges, and future perspectives, *Separ. Purif. Rev.*, 2026, 1–26.

10 N. Jamila, R. Ullah, F. Khitab, N. Ahmad, F. Ahmad, A. M. Siddique, *et al.*, Visible-light-sensitive highly-efficient photocatalytic degradation of hazardous contaminant fast yellow AB in industrial wastewater using zinc ferrite nano-photocatalyst: synthesis, characterization and removal performance, *Spectrosc. Lett.*, 2025, 1–15.

11 E. Fouad, F. Ahmad and N. Ahmed, Optimization of chromium extraction from aqueous solutions by emulsion liquid membrane, *Desalination Water Treat.*, 2017, **65**, 428–434.

12 Y. Yue, X. Yue, X. Tang, L. Han, J. Wang, S. Wang, *et al.*, Synergistic adsorption and photocatalysis study of TiO_2 and activated carbon composite, *Heliyon*, 2024, **10**(10), e30817.

13 E. Kusiak-Nejman, A. Sienkiewicz, A. Wanag, P. Rokicka-Konieczna and A. W. Morawski, The role of adsorption in the photocatalytic decomposition of dyes on APTES-Modified TiO_2 nanomaterials, *Catalysts*, 2021, **11**(2), 172.

14 W. S. Al-Arjan, Zinc oxide nanoparticles and their application in adsorption of toxic dye from aqueous solution, *Polymers*, 2022, **14**(15), 3086.

15 N. Hussain, M. Asif, S. Shafaat, M. S. Khan, N. Riaz, M. Iqbal, *et al.*, Multilayer adsorption of reactive orange 16 dye onto Fe_2O_3/ZnO hybrid nanoadsorbent: mechanistic insights from kinetics, isotherms and dynamic light scattering studies, *J. Chem. Technol. Biotechnol.*, 2025, **100**(1), 50–66.

16 A. A. Ati, A. H. Abdalsalam and A. S. Hasan, Thermal, microstructural and magnetic properties of manganese substitution cobalt ferrite prepared via co-precipitation method, *J. Mater. Sci.: Mater. Electron.*, 2021, **32**(3), 3019–3037.

17 N. Hussain, S. Shafaat, A. Sarfraz, M. Usman, M. S. Khan, A. M. Khan, *et al.*, Engineered hybrid iron-cobalt metal oxide nanoparticles for effective adsorption of malachite green dye, *J. Chem. Technol. Biotechnol.*, 2024, **99**(12), 2553–2568.

18 C. Erhonyota, G. I. Edo and F. O. Onoharigho, Comparison of poison plate and agar well diffusion method determining the antifungal activity of protein fractions, *Acta Ecol. Sin.*, 2023, **43**(4), 684–689.

19 B. Yalcin, S. Ozcelik, K. İçin, K. Senturk, B. Ozcelik and L. Arda, Structural, optical, magnetic, photocatalytic activity and related biological effects of $CoFe_2O_4$ ferrite nanoparticles, *J. Mater. Sci.: Mater. Electron.*, 2021, **32**(10), 13068–13080.

20 K. Kombaiah, J. J. Vijaya, L. J. Kennedy, M. Bououdina, R. J. Ramalingam and H. A. Al-Lohedan, Comparative investigation on the structural, morphological, optical, and magnetic properties of $CoFe_2O_4$ nanoparticles, *Ceram. Int.*, 2017, **43**(10), 7682–7689.

21 Y. I. Choi, Y.-I. Kim, D. W. Cho, J.-S. Kang, K. Leung and Y. Sohn, Recyclable magnetic $CoFe_2O_4$/BiOX (X= Cl, Br and I) microflowers for photocatalytic treatment of water contaminated with methyl orange, rhodamine B, methylene blue, and a mixed dye, *RSC Adv.*, 2015, **5**(97), 79624–79634.

22 A. Manikandan, M. Durka, K. Seevakan and S. A. Antony, A novel one-pot combustion synthesis and opto-magnetic properties of magnetically separable spinel $Mn_xMg_{1-x}Fe_2O_4$ ($0.0 \leq x \leq 0.5$) nanophotocatalysts, *J. Supercond. Novel Magn.*, 2015, **28**(4), 1405–1416.

23 J. Revathi, M. J. Abel, V. Archana, T. Sumithra and R. Thiruneelakandan, Synthesis and characterization of $CoFe_2O_4$ and Ni-doped $CoFe_2O_4$ nanoparticles by chemical Co-precipitation technique for photo-degradation of organic dyestuffs under direct sunlight, *Phys. B*, 2020, **587**, 412136.

24 J. S. de Oliveira, J. d. S. Salla, R. C. Kuhn, S. L. Jahn and E. L. Foletto, Catalytic ozonation of melanoidin in aqueous solution over $CoFe_2O_4$ catalyst, *Mater. Res.*, 2018, **22**(1), e20180405.

25 L. Wu, G. Wan, N. Hu, Z. He, S. Shi, Y. Suo, *et al.*, Synthesis of porous $CoFe_2O_4$ and its application as a peroxidase mimetic for colorimetric detection of H_2O_2 and organic pollutant degradation, *Nanomaterials*, 2018, **8**(7), 451.

26 M. Qasim, K. Asghar and D. Das, Preparation and characterization of $CoFe_2O_4$ and $CoFe_2O_4$@ Albumen nanoparticles for biomedical applications, *Ceram. Int.*, 2019, **45**(18), 24971–24981.

27 C. Simonescu, A. Tătăruș, D. Culiță, N. Stănică, I. Ionescu, B. Butoi, *et al.*, Comparative Study of $CoFe_2O_4$ Nanoparticles and $CoFe_2O_4$-Chitosan Composite for Congo Red and Methyl Orange Removal by Adsorption, *Nanomaterials*, 2021, **11**, 711.

28 M. A. Ansari, R. Govindasamy, M. Y. Begum, M. Ghazwani, A. Alqahtani, M. N. Alomary, *et al.*, Bioinspired ferromagnetic $CoFe_2O_4$ nanoparticles: potential pharmaceutical and medical applications, *Nanotechnol. Rev.*, 2023, **12**(1), 20230575.

29 A. S. Abdulhameed, A.-T. Mohammad and A. H. Jawad, Modeling and mechanism of reactive orange 16 dye adsorption by chitosan-glyoxal/TiO_2 nanocomposite: application of response surface methodology, *Desalination Water Treat.*, 2019, **164**, 346–360.

30 W. Saeed, Z. Abbasi, M. Bilal, S. H. Shah, A. Waseem and A. J. Shaikh, Interactive behavior of graphene quantum dots towards noble metal surfaces, *Physica E Low Dimens Syst Nanostruct.*, 2023, **147**, 115596.

31 M. Usman, A. Sarfraz, S. Shafaat, N. Hussain, A. M. Khan, Z. Hussain, *et al.*, A multiparametric study for size and stability of hybrid Fe_2O_3-NiO nanoparticles and their statistical transformation, *Part. Sci. Technol.*, 2024, **42**(7), 1282–1301.

32 C. Iacovita, A. Florea, R. Dudric, E. Pall, A. I. Moldovan, R. Tetean, *et al.*, Small versus large iron oxide magnetic nanoparticles: Hyperthermia and cell uptake properties, *Molecules*, 2016, **21**(10), 1357.

33 D. Gheidari, M. Mehrdad, S. Maleki and S. Hosseini, Synthesis and potent antimicrobial activity of $CoFe_2O_4$ nanoparticles under visible light, *Heliyon*, 2020, **6**(10), e05058.

34 P. S. Kumar and R. Gayathri, Adsorption of Pb^{2+} ions from aqueous solutions onto bael tree leaf powder: isotherms, kinetics and thermodynamics study, *J. Eng. Sci. Technol.*, 2009, **4**(4), 381–399.

35 S. Yavari, N. M. Mahmodi, P. Teymouri, B. Shahmoradi and A. Maleki, Cobalt ferrite nanoparticles: preparation, characterization and anionic dye removal capability, *J. Taiwan Inst. Chem. Eng.*, 2016, **59**, 320–329.

36 Z. Zaheer, W. A. Bawazir, S. M. Al-Bukhari and A. S. Basaleh, Adsorption, equilibrium isotherm, and thermodynamic studies to the removal of acid orange 7, *Mater. Chem. Phys.*, 2019, **232**, 109–120.

37 K. H. Shah, M. Fahad, S. Ali, A. Batool, I. Shah, U. Farooq, *et al.*, Potential of natural ferruginous manganese (NFM) ore as a natural adsorbent for As (III) removal at low concentration, *Int. J. Environ. Anal. Chem.*, 2021, 1–18.

38 A. S. Abdulhameed, A.-T. Mohammad and A. H. Jawad, Application of response surface methodology for enhanced synthesis of chitosan tripolyphosphate/TiO_2 nanocomposite and adsorption of reactive orange 16 dye, *J. Clean. Prod.*, 2019, **232**, 43–56.

39 G. S. Aljeddani, R. M. Alghanmi and R. A. Hamouda, Study on the isotherms, kinetics, and thermodynamics of adsorption of crystal violet dye using Ag-NPs-loaded cellulose derived from peanut-husk agro-waste, *Polymers*, 2023, **15**(22), 4394.

40 M. Perwez, H. Fatima, M. Arshad, V. Meena and B. Ahmad, Magnetic iron oxide nanosorbents effective in dye removal, *Int. J. Environ. Sci. Technol.*, 2023, **20**(5), 5697–5714.

41 D. Sun, Z. Zhang, M. Wang and Y. Wu, Adsorption of reactive dyes on activated carbon developed from Enteromorpha prolifera, *Am. J. Anal. Chem.*, 2013, **4**(7A), 17–26.

42 O. Duman and E. Ayranci, Structural and ionization effects on the adsorption behaviors of some anilinic compounds from aqueous solution onto high-area carbon-cloth, *J. Hazard. Mater.*, 2005, **120**(1), 173–181.

43 A. M. Hardieka and T. B. Budak, Investigation of Removing Basic Yellow 28 and Basic Blue 3 Dyes from Water Using Mulberry Leaves (Morus nigra L.) and Assessment of Ultrasonic Effects, *Molecules*, 2025, **30**(17), 3539.

44 D. Yanardag, G. G. Kaya and S. Edebali, Ciprofloxacin adsorption performance of Co-doped UiO-66, *Appl. Organomet. Chem.*, 2024, **38**(1), e7311.

45 E. Ayranci and O. Duman, In-situ UV-visible spectroscopic study on the adsorption of some dyes onto activated carbon cloth, *Sep. Sci. Technol.*, 2009, **44**(15), 3735–3752.

46 O. Duman and E. Ayranci, Adsorption Characteristics of Benzaldehyde, Sulphanilic acid, and p-Phenolsulfonate from Water, Acid, or Base Solutions onto Activated Carbon Cloth, *Sep. Sci. Technol.*, 2006, **41**(16), 3673–3692.

47 I. Ahmed and M. Gasser, Adsorption study of anionic reactive dye from aqueous solution to Mg–Fe–CO_3 layered double hydroxide (LDH), *Appl. Surf. Sci.*, 2012, **259**, 650–656.

48 V. J. Inglezakis and A. A. Zorpas, Heat of adsorption, adsorption energy and activation energy in adsorption and ion exchange systems, *Desalination Water Treat.*, 2012, **39**(1–3), 149–157.

49 J. Xu, X. Shen, D. Wang, C. Zhao, Z. Liu, I. P. Pozdnyakov, *et al.*, Kinetics and mechanisms of pH-dependent direct photolysis of p-arsanilic acid under UV-C light, *Chem. Eng. J.*, 2018, **336**, 334–341.

50 N. Ali, A. Said, F. Ali, F. Raziq, Z. Ali, M. Bilal, *et al.*, Photocatalytic degradation of congo red dye from aqueous environment using cobalt ferrite nanostructures: development, characterization, and photocatalytic performance, *Water, Air, Soil Pollut.*, 2020, **231**(2), 50.

51 A. Saleem, H. Khan, S. M. Bukhari, L. B. Tahar, U. Farooq and A. J. Shaikh, Lone Pair versus Aromatic Interactions on Metal Oxide Surfaces: A Combined Spectroscopic and Computational Study, *Dalton Trans.*, 2025, **54**, 16508–16524.

52 A. Baratov, Z. Kuspanov, A. Shaimerdenov, G. Yergaziyeva, Y. Yerlanuly and C. Daulbayev, Enhancing photogenerated charge separation in perovskite semiconductors via dual cocatalyst engineering, *J. Water Proc. Eng.*, 2025, **77**, 108573.

53 A. H. Navidpour, M. B. Ahmed and J. L. Zhou, Photocatalytic degradation of pharmaceutical residues from water and sewage effluent using different TiO_2 nanomaterials, *Nanomaterials*, 2024, **14**(2), 135.

54 M. Y. Afzal, M. Bilal, H. Khan, M. Asif, M. S. Khan, M. Iqbal, *et al.*, Understanding Photocatalytic Degradation of RB5 Dye under Salts Using Nickel Sulfide Nanoparticles: Insights from Dynamic Light Scattering and Theoretical Investigations, *ACS Omega*, 2025, **10**(30), 32918–32938.

55 M. Saqib, F. Shafiq, W. Qiao, F. Shah and A. M. Khan, Interfacial engineering of Mn-ZnO/g-C_3N_4 heterostructure for selective mixed dye degradation under visible light, *J. Alloys Compd.*, 2026, 187156.

56 U. Song, H. Jun, B. Waldman, J. Roh, Y. Kim, J. Yi, *et al.*, Functional analyses of nanoparticle toxicity: a comparative study of the effects of TiO2 and Ag on tomatoes (Lycopersicon esculentum), *Ecotoxicol. Environ. Saf.*, 2013, **93**, 60–67.

57 M. L. López-Moreno, L. L. Avilés, N. G. Pérez, B. Á. Irizarry, O. Perales, Y. Cedeno-Mattei, *et al.*, Effect of cobalt ferrite ($CoFe_2O_4$) nanoparticles on the growth and development of Lycopersicon lycopersicum (tomato plants), *Sci. Total Environ.*, 2016, **550**, 45–52.

58 A. J. Shaikh, M. Batool, M. A. Yameen and A. Waseem, Plasmonic Effects, Size and Biological Activity Relationship of Au-Ag Alloy Nanoparticles, *J. Nano Res.*, 2018, **54**, 98–111.

59 Antibacterial activity of cobalt ferrite ($CoFe_2O_4$) nanoparticles against oral enterococci, *Materials Science Forum*, ed. Sulaiman J. M., Hamdoon S. M., Abdulrahman G. Y., Trans Tech Publ, 2021.

60 V. Srivastava, T. Kohout and M. Sillanpää, Potential of cobalt ferrite nanoparticles ($CoFe_2O_4$) for remediation of hexavalent chromium from synthetic and printing press wastewater, *J. Environ. Chem. Eng.*, 2016, **4**(3), 2922–2932.